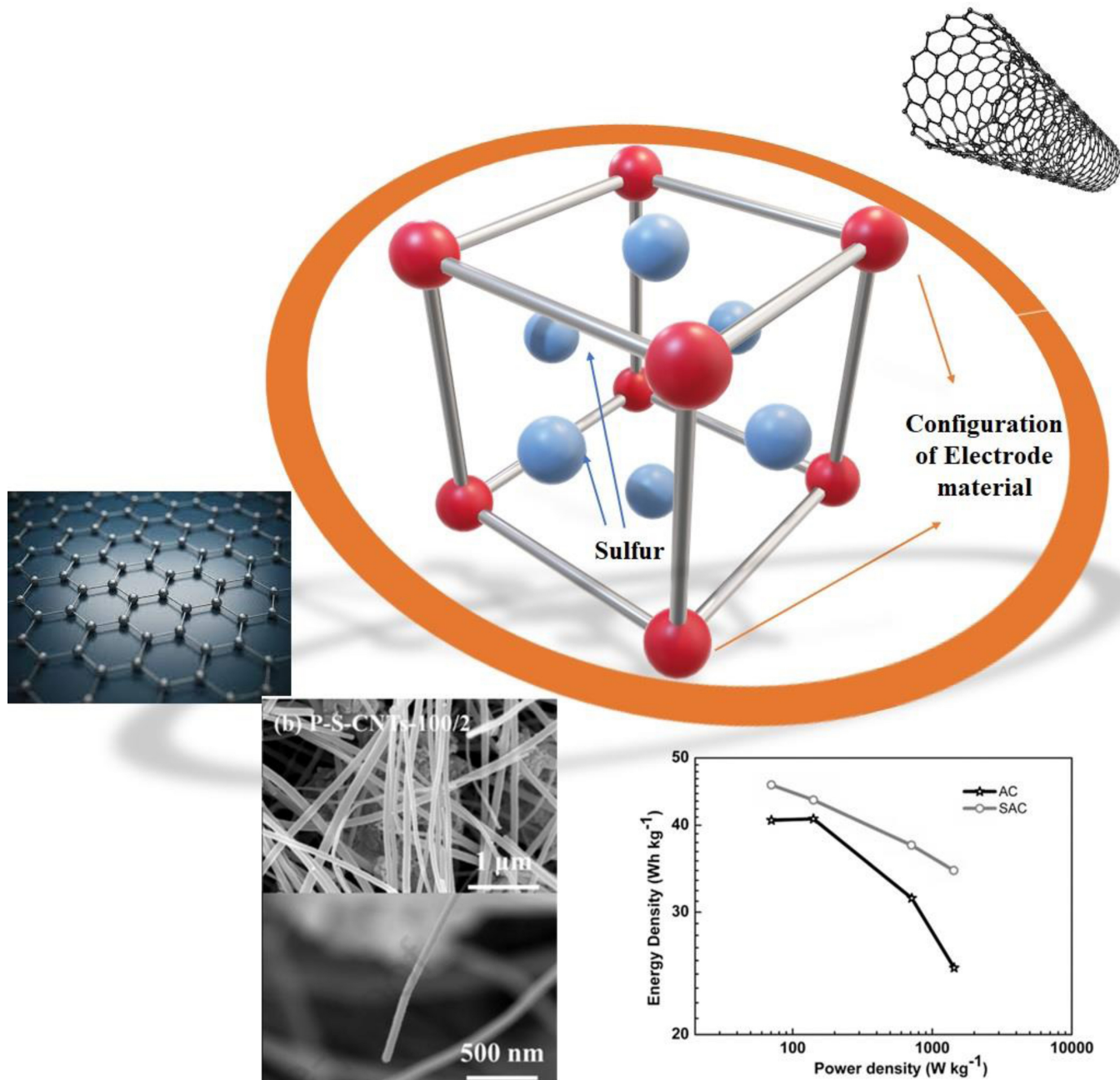


Sulfurization of Electrode Material: A Promising Window for Supercapacitor Technology

Junaid Khan,^{*[a, b]} Noshaba Shakeel,^[c] Shahid Alam,^[c] Faiz Alam,^[a] and Alaa Dahshan^[d]



Supercapacitors have emerged as a promising energy storage technology with attributes like high power and tuneable energy density along with splined cyclic potential. Their performance is heavily driven by the employed electrode materials that still crave high charge storage and rate capabilities as well as virile conductivity. Among numerous applied strategies to patch the corresponding quandary, sulfurization has garnered significant attention as an effective method for improving the electrochemical depiction of electrode materials. This review article presents a comprehensive analysis of the sulfurization process applied to the electrode with the aim of providing profound overview of the latest developments, the impact of sulfur

incorporation on electrode properties, and the resulting performance enhancement in supercapacitors. It explores the influence of sulfidation on the morphological, structural, and compositional aspects of electrode materials, highlighting the modification of surface area, pore size distribution, crystal structure, and the formation of active sites. The discussions on the improved specific capacitance, enhanced rate capability, prolonged cycle life, and upgraded energy density achieved are accumulated. Additionally, the review explores the challenges and limitations associated with sulfurization and strategies to mitigate trials for future directions of research and developments.

1. Introduction

The world's energy consumption has been escalating at a concerning pace, primarily driven by the continued combustion of fossil fuels.^[1] The surge in global population has led to a corresponding increase in the demand for energy worldwide. Despite this escalating demand, the current energy production and available supplies have struggled to keep pace with the growing population and its heightened energy needs.^[2] Alarming global and environmental challenges consequently, demand for clean energy solutions to foster the development of a sustainable society.^[3] The potential presence of renewable energy resources further strengthens the progression but their constraint availability makes it unachievable without efficient and long-lasting energy storage systems.^[4] Supercapacitors (Sc)^[5] and batteries are a pair of electrochemical energy-storage devices that are widely used for corresponding tasks and are considered among the most promising storage systems.^[6] In Batteries, charge storage occurs through redox reactions between the active materials and the electrolyte which provide them efficient specific energy enrichment but also import frail cyclic performance and low specific power.^[7] The two main classifications of Sc are Electrostatic double-layer capacitors (EDLC) and Pseudocapacitors. In EDLC formation of an electrostatic double-layer via adsorption/desorption of ionic species results in the storage of charge.^[8] The Purely electrostatic storage phenomena not only enable fast charge and discharge rates but also incorporate excellent stability characters to Sc.^[9] Carbonaceous materials including Graphene, Carbon nano-

tubes, and Activated carbon are employed as electrode materials for EDLC applications.^[10] Pseudocapacitance involves rapid reversible redox reactions at the electrode-electrolyte interface, allowing for additional charge storage beyond the double-layer capacitance.^[11] Conducting polymers and few Metal oxides are materials that bear pseudocapacitive nature.^[12] Compared to batteries, Sc store less energy per unit mass or volume which restricts their ability to provide long-term energy storage solutions.^[13] The incorporation of hybrid chemistries (a combination of electrostatic and redox activities) in Sc technology (hybrid Sc) has opened a window to procure the synergistic status between Sc and rechargeable batteries.^[14] The recent developments in hybrid Sc and their profited attributes (high specific power and energy density along with stable cyclic performance) have stated them the promising choice for future energy storing technologies.^[15]

The most recently employed electrode materials for stated tasks are carbon nanotubes, activated carbon, graphene, transition metal phosphatase, hydroxides, oxides and metal-organic frameworks MOFs.^[16,17] The pure approach for the implementation of these materials in practical assemblies has not yet achieved the expected (theoretical) outcomes.^[18] The limited storage capacity, slow reaction kinetics, cycling degradation, frail rate capability, and insufficient energy density have been the most common challenges to overcome.^[19] Numerous approaches like post-synthesis modifications,^[20] doping/compositing, nanostructuring, surface modification, hybridization, advancements in the electrolytic environment, interface engineering, and in-situ strategy have been tested.^[21-23] With the enhancement in energy storage profits, each approach imports certain constraints that demand a nascent and fresh approach. Sulfurization of electrode components has attracted a lot of interest in recent years.^[24] The incorporation of sulfur species enhances the electrochemical performance by providing additional pseudocapacitive behaviour, promoting charge storage through redox reactions, and raising the material specific capacitance (Cs).^[25] In addition, Sulfurization alters the surface properties of electrode materials. It can lead to the formation of active sites, increase surface roughness, and modify the surface chemistry of the electrode, facilitating improved charge transfer kinetics and enhancing overall electrochemical performance.^[26] This is particularly important for applications that require high power output or fast energy delivery. Combining sulfurization

[a] J. Khan, F. Alam

Department of Physics
Government Postgraduate Collage No. 1
Abbottabad, Khyber Pakhtunkhwa (Pakistan)
E-mail: junaidkhan.nanotech@gmail.com

[b] J. Khan

Department Of Higher Education Achieves and Libraries
Government of Khyber Pakhtunkhwa (Pakistan)

[c] N. Shakeel, S. Alam

Abbottabad University of Science and Technology
Khyber Pakhtunkhwa (Pakistan)

[d] A. Dahshan

Department of Physics – Faculty of Science
King Khalid University
P.O. Box 9004, Abha (Saudi Arabia)

with nanostructuring or surface modification techniques can further enhance the electrochemical properties of electrode materials, leading to improved performance in energy storage devices.^[27] Moreover, sulfur possesses a lone pair of electrons, when introduced in electrode material influences the pore size, structure, and capacitance behaviour of electrode materials.^[28] Conjugating the lone pair on the heteroatoms with the carbon framework system can enhance the wettability of electrolytes and improve surface activity, including the faradaic nature. Enhancements in the redox properties directly contribute to the elevation of capacitance, conductivity, and rate capability of electrode materials.^[29] These discussed features as presented in Figure 1 demonstrate the sulfurization of electrode material as the promising future of supercapacitor technology.

Many significant results of the sulfidation process along with diverse synthetic approaches have been reported recently but thus far no review article has been reported to provide a comprehensive itinerary. The choice of materials, their morphology, dimension and synthesis techniques, along with their collaboration with other components within the supercapacitor device, stand out as crucial factors. This research article intends to offer a comprehensive analysis of the sulfurization technique for high-performance Scs. The various sulfurization methods employed have been discussed along with recent advancements and highlights has been discussed. Additionally, the

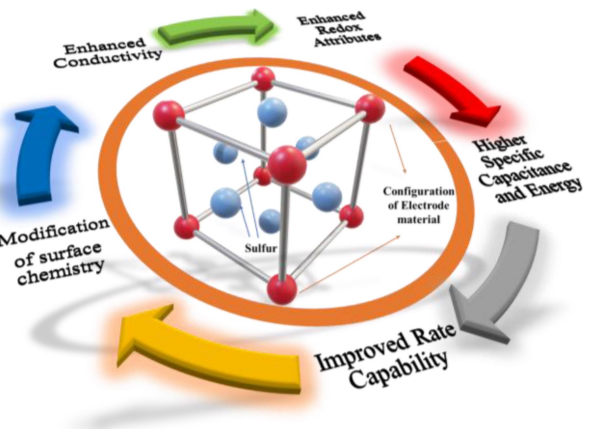


Figure 1. Schematic illustration of exported attributes as a result of sulfurization of electrode material.

challenges and prospects associated with the implementation of sulfurization techniques in practical Sc devices have been discussed to provide a pathway for future work. Overall, this research article intends to provide valuable information about the sulfurization of Sc electrode materials, with the eventual objective of improving the storage of energy performance and enabling the development of highly efficient Sc systems.



Junaid Khan, an independent researcher currently affiliated with Department Of Higher Education Achieves and Libraries, Government of Khyber Pakhtunkhwa, Pakistan. He is working as Lecturer in Physics at Department of Physics, Abbottabad University of Science and Technology, Khyber Pakhtunkhwa, Pakistan. His research interest relates with synthesis of nanomaterial, Nanoscale engineering, Energy storage, and Water splitting (Google Scholar ID: https://scholar.google.com/citations?user=Dq_vEUcAAAAJ&hl=en.



Noshaba Shakeel, a brilliant student perusing his MS from Abbottabad University of Science and Technology, Khyber Pakhtunkhwa, Pakistan.



Shahid Alam, Assistant professor at Department of Physics, Abbottabad University of Science and Technology, Khyber Pakhtunkhwa, Pakistan. His research interest relates with synthesis of nanomaterial and Energy storage.



Faiz Alam Jadoon, Associate Professor at Department of Physics, Government Postgraduate Collage No.1, Abbottabad, Khyber Pakhtunkhwa, Pakistan. His research interest relates with synthesis of nanomaterial and Energy storage.



Alaa Dahshan, professor at Department of Physics – Faculty of Science – King Khalid University, P.O. Box 9004, Abha, Saudi Arabia. His research interest relates with synthesis of nanomaterial.

2. Synthetic Approach

The synthetic approach used for electrode material fabrication plays a crucial role in determining its properties, performance, and overall suitability for energy storage applications. It determines the morphology and nanostructure of electrode materials. Controlling particle size, shape, and distribution can significantly impact the surface area, porosity, and accessibility of active sites, which are crucial for efficient charge storage and transport. Different crystal structures can exhibit varying electrochemical properties, such as higher ion diffusion rates or increased stability, making phase control essential for optimizing performance. An effective synthetic approach ensures the scalability and reproducibility of electrode materials. It allows for the production of electrode materials in large quantities while maintaining consistent properties and performance across different batches, facilitating their practical application and commercialization. Several reported routes are employed for sulfurization among which the most significant are:

2.1. Hydrothermal method

Hydrothermal synthesis is a technique used to fabricate materials under high-temperature and high-pressure conditions in an aqueous environment. It involves placing precursors or reactants in a sealed vessel filled with a solvent, typically water, and subjecting them to elevated temperatures, usually ranging from 100 to 300 degrees Celsius. Hydrothermal assembly was employed by D. Wu et al. to create sulphur and nitrogen co-doped graphene hydrogels.^[30] A typical aqueous graphene oxide GO dispersion containing methionine of 30 mg, which has a mass ratio of 0.5:1 to GO, was subjected to 30 minutes of sonication. After then, the mixture underwent another 30 minutes of magnetic stirring. After being sealed in an autoclave lined with Teflon, the resulting stable suspension underwent a 4-hour hydrothermal treatment at 160 °C. The autoclave was then allowed to naturally cool to room temperature in order to get rid of any unreacted chemicals. The NS-G hydrogel produced was then removed and placed in deionized water. The aerogel NS-Gm05 was then created by overnight freeze-drying the NS-G hydrogel. The resulting samples were compared along with the methionine to GO ratio of 0.5:1 and are known as NS-Gm01 and NS-Gm1, respectively. These extra mass ratios were used employing the identical synthesis procedure, were 0.1:1 and 1:1. N. Poompiev et al. fabricate nickel cobalt sulfide (NCS) nanostructures on sulfur and nitrogen dual-doped graphene (SN-G) surfaces using an easy, two-step *in situ* hydrothermal method.^[31] In the presence of graphene oxide and thiourea, a moderate procedure of hydrothermal results in the crystallinity, form, and crystal structure of an intermediate combination of cobalt carbonate hydroxides and nickel. The electrochemical performance, cyclic stability, and capacitive rate performance of nitrogen and sulfur co-doped graphene surfaces were investigated to assess the impacts of their cohabitation. In order to use hybrid Scs, NCS/NS-G composites are being researched as a possible good choice. In their study,

S. Uppugalla et al. utilized a conventional approach by introducing 300 mg of activated carbon into 100 mL of distilled water to achieve effective results.^[32] In 60 mL of water, a specific amount of NH₄SCN was dissolved before the aforementioned emulsion was introduced and stirred for 5 minutes. The mixture that emerged from this was kept in a 250 mL stainless steel autoclave. The autoclave was subjected to a 10-hour hydrothermal treatment at 180 °C before being allowed to naturally cool to a suitable temperature. This mixture was bathed with acetone and deionized water to eliminate any last unaltered substances. To further characterize the sample, it was subjected to dehydration in an oven maintained at a temperature of 60 °C. Three separate specimen were produced utilizing 3, 1.5 and 0.75 g of NH₄SCN these specimens are known as, NSAC-3, NSAC-2 and NSAC-1 correspondingly. The same technique was used to produce hydrothermally treated activated carbon (HTAC) utilising only activated carbon and no NH₄SCN.

2.2. Solvothermal method

The solvothermal method is a synthetic technique used to produce materials under high-temperature and high-pressure conditions using a solvent as the reaction medium. It is similar to hydrothermal synthesis but typically involves non-aqueous solvents instead of water. J. Huo et al. created Sulphur/Nitrogen co-doped rGO (SNG) hydrogels using a solvothermal technique utilizing 3-dimensional SNG hydrogels made from GO (produced using an improved Hummers' method).^[33] A 2 mg/mL solution of GO powder was first made by evenly dissolving it in EG using an ultrasonic method. Following that, a quantity of 2 mM of L-cysteine was introduced into the combined solution, which was subsequently stirred at a temperature of 70 °C for a duration of 0.5 hours. After that, the mixture was placed in a hydrothermal reactor, where bears 180 °C temperature for 12 hours. Once the temperature fell to room temperature, the Sulphur/Nitrogen co-doped rGO (SNG) hydrogels were cleaned in 500 mL of a 9:1 ethanol solution and deionized water. The formation of the SNG aerogels required freeze-drying for 48 hours. To create the binder-free SNG, a piece of the SNG aerogel was divided into two and applied to a square of nickel foam (1×1 cm²). Y. Hu et al. used the same solvothermal process for preparing Nickel cobalt sulfides (NiCo₂S₄) electrode for Sc in order to create a homogenous solution.^[34] First, 4 g of thiourea was mixed in 20 mL of PEG 200 and agitated for an hour. Subsequent to a stirring period of 1.5 hours, then previously mentioned solution was dissolved in 1.455 g of Ni(NO₃)₂·6H₂O along with 2.91 g of Co(NO₃)₂·6H₂O. The resulting composition was poured into an autoclave with a Teflon liner that held 100 mL. The autoclave was heated to 160 °C for 16 hours before being allowed to cool down. After ethanol, deionized water and centrifuging were used to clean the resultant black precipitate three times. Finally, NiCo₂S₄ which resembled an urchin was created by drying the sample for a whole night at 60 °C under vacuum. H. Chen and colleagues used a straightforward template-free method that combines solvothermal synthesis in ethylene glycol with subsequent annealing in the air.^[35] In the

modified Hummer's technique, graphite powder was employed as the first component by H. Deng et al. to create nitrogen and sulfur co-doped graphene (NSG) electrodes for Sc.^[36] The NSG (Nitrogen and Sulfur co-doped Graphene) was synthesized utilizing the solvothermal approach. The GO (Graphene Oxide) (100 mg) and thiourea (1 g) were curated for two hours. The mixture was then subjected to sonication for a day, in a 200 mL dry autoclave, the mixture was then heated to 150 °C overnight. Centrifuging the mixture, washing it three to five times with deionized water, and finally freeze-drying it for 36 hours were all done after the mixture had cooled to between 20 and 30 °C. The final step required heating the collected intermediates in an argon atmosphere for three hours at 800 °C. In contrast, using the same technique but without thiourea, undoped graphene (UG) was produced.

2.3. Sonochemical method

The sonochemical method, also known as ultrasonic-assisted synthesis or ultrasonic irradiation, is a technique used for the synthesis and processing of materials using high-frequency sound waves. It involves the application of ultrasound waves in a liquid medium to induce various physical and chemical effects, leading to the formation or modification of materials. Using a straightforward sonochemical method, N. Karthik et al. created sulfur-doped copper-nickel hydroxides with various morphologies by precisely controlling the volumetric concentration of thiourea (the sulfur source).^[37] The pseudo-capacitive characteristics of the hybrid foams were subsequently evaluated. One of the hybrid foams with the greatest Cs was selected for the reduction degradation of methyl orange (MO) and congo red (CR) in the presence of sodium borohydride. As a result, the TU-6 hybrid demonstrates promising specific capacitive performance, and the catalytic activity strongly confirms the combined benefits of the hydroxide shell and sulfur core, indicating synergistic effects. Sulfur-doped copper-nickel hydroxides represent a promising strategy for addressing energy and environmental challenges, although their overall applicability may be contingent upon their impact. J. Acharya et al. CoFe₂O₄/MWCNT hybrids with different MWCNT concentrations (20, 15, 10, and 5 mg for CFC20, CFC15, CFC10, and CFC5, respectively) were effectively made and working as an electrode material for Sc applications using an ultrasound-assisted sonochemical technique.^[38] We investigated the effects of MWCNT meditations on the performances and morphologies of CoFe₂O₄/MWCNT hybrids with well-distributed MWCNTs. The hybrids of CoFe₂O₄ and MWCNTs with a concentration of 15 mg MWCNTs demonstrated exceptional rate capability, stability, and 390 F/g Cs. The asymmetric Sc device demonstrated 26.7 Wh/kg at high power densities (319 W/kg). It was produced utilizing the negative electrode material activated carbon and as the positive electrode CFC15. Ultrasonic exfoliation was suggested by C. Bathula et al. A glass vial containing 50 mg of polymer PDT and 20 mL of toluene was stirred with an ultrasonic probe for 10 min to produce a fine solution.^[39] The mixture was sonicated at 50% amplitude for 1 hour to achieve

PDPT-CNT. After sending CNTs in 5 mL of toluene at a concentration of 1 mg/mL. To eliminate any unassembled CNT sheets or polymer, the final mixture was centrifuged three times for 30 minutes at 11,000 rpm. After that, it was washed many times with acetone and water. The PDPT-CNT was dried at 60 °C for 4 hours to produce the end product. A vacuum desiccator was used to hold the completed product for further characterization and electrochemical research.

2.4. Solgel method

The sol-gel method is a versatile and widely used technique for the synthesis of inorganic and hybrid materials, such as metal oxides, glasses, ceramics, and composites. It involves the conversion of a sol (a stable colloidal suspension) into a gel through controlled hydrolysis and condensation reactions. C. Han et al. modified the sol-gel preparation technique to assess how the choice of solvent affected the synthesis of sulfur-doped, visible light-activated TiO₂.^[40] Polyoxyethylene (80) sorbitan monooleate, often referred to as Tween 80, was utilized as a pore-directing reagent and is available from Sigma-Aldrich. The preparation of several sol-gels used four distinct solvents as principal solvents methanol, ethanol, isopropane, and 1-butanol. As an alkoxide precursor, titanium isopropoxide was added to the mixes of Tween 80 and the respective solvents after the surfactant had been dissolved in the solvents. Sulfuric acid, a precursor to sulfur and a reagent that creates water through an esterification reaction with the solvent was further added. J. Huo et al. employed the sol-gel method to synthesize a foam composed of dual-doped reduced graphene oxide (SNG).^[41] Subsequently, the SNG material is immersed in an aqueous solution of TiO₄ to facilitate the formation of mesoporous anatase TiO₂ nanoparticles on its surface under low-temperature conditions. This sustainable preparation method didn't call for any further annealing. In this scenario, the co-doping of sulfur and nitrogen (S/N) proves to be highly effective in enhancing the chemical and electrical properties of the SNG material. The resulting 3D-structural TiO₂/SNG composite material provides a greater specific surface area and improved structural stability. The presence of TiO₂ nanoparticles effectively enhances the availability of active sites for Li⁺ ion insertion and extraction processes, while simultaneously mitigating the stacking and agglomeration of SNG sheets. The presence of mesoporous structures expands the contact area between the electrolytes and the electrodes, while the incorporation of TiO₂ nanoparticles reduces the diffusion distance of Li⁺ ions. When utilized as the anode materials in lithium-ion batteries (LIBs), the SNG/TiO₂ composite exhibits consistent cycling performance, exhibiting both high reversible capacity and exceptional rate capability. Sulfur-doped carbon spheres were effectively produced by H. Tang et al. with hierarchical micro/mesopores (S-MCSs) using a two-step process that combined the Stober method with a sol-gel procedure using the cationic surfactant cetyltrimethylammonium bromide (CTAB) as a template.^[42] In an alkaline environment, the carbon source resorcinol formaldehyde (RF) is employed, along with

tetraethyl orthosilicate (TEOS) as an additional pore-forming agent. Sulfur is then added to the combination while it is heated. The synthesized S-MCSs exhibit remarkable cycle stability and a high reversible capacity as anode materials for SIBs.

3. Sulfurized Electrode Materials

Various types of electrode materials have been explored for sulfurization with an aim in supercapacitor applications. Here are some of the most explored electrode materials that undergo sulfurization:

3.1. Sulfidation profits among carbonaceous materials

3.1.1. Activated carbon

The fascinating feather of sulfurization in terms of electrochemical performance ignited the researchers interest significantly in the recent decade. Recently many energy storage systems based on sulfurized activated carbon have been scrutinized to streamline their path for practical implementation. According to Y. Huang et al. pyrolyzing sulphur flakes produced sulfurized activated carbon (SAC).^[43] When the surface of the pores was analyzed using surface characterization methods, the presence of thiophenic sulfur functional groups was observed. The presence of 2.7% sulfur content within the material is evident through the utilization of X-ray photoelectron spectroscopy (XPS). SEM images of the cross sections

for the unmodified and S-modified AC samples show the surface morphologies of the AC and SAC samples show no significant differences with macropores in both. Notably, the SAC samples retain their porous structure after undergoing sulfur modification. Figure 2(a) displays the cyclic voltammetry (CV) curves of sulfurized and non-sulfurized activated carbon, recorded using a 10 mV/s scan speed. The quasi-rectangular shapes evidence the capacitive nature. Compared to the AC sample, the SAC sample occupies a larger area under the curve, which portrays dominant capacitive behaviour as compared to AC. The understanding of profited performance is clear in EIS measurements (Figure 2b) which indicate improved conductivity via the incorporation of sulfur. The decreased interfacial charge transfer resistance (R_{ct}) is seen along an ESR value of 8.2 Ω for SAC and small semicircles at high frequency region, evincing a better conductive impact as compared with AC (10.6 Ω ESR). The impedance graphs for both samples were simulated using the analogous circuit depicted in the inset of Figure 2(b). The complex plane impedance values were generated through a computational process that again depicts the improve conductivity vis sulfidation. Figure 2(c) illustrates that the SAC samples exhibited superior performance in terms of E_s and P_s when compared to the AC sample. Based on the meticulous examination of the data depicted in Figure 2, it is evident that the SAC sample exhibits superior performance compared to the AC samples concerning E_s and P_s . Comparing the SAC sample to the unmodified AC sample, it is evident that the SAC sample demonstrated superior conductivity. This conclusion is based on the formal analysis of the C_s values indicates that the SAC samples exhibit higher capacitance

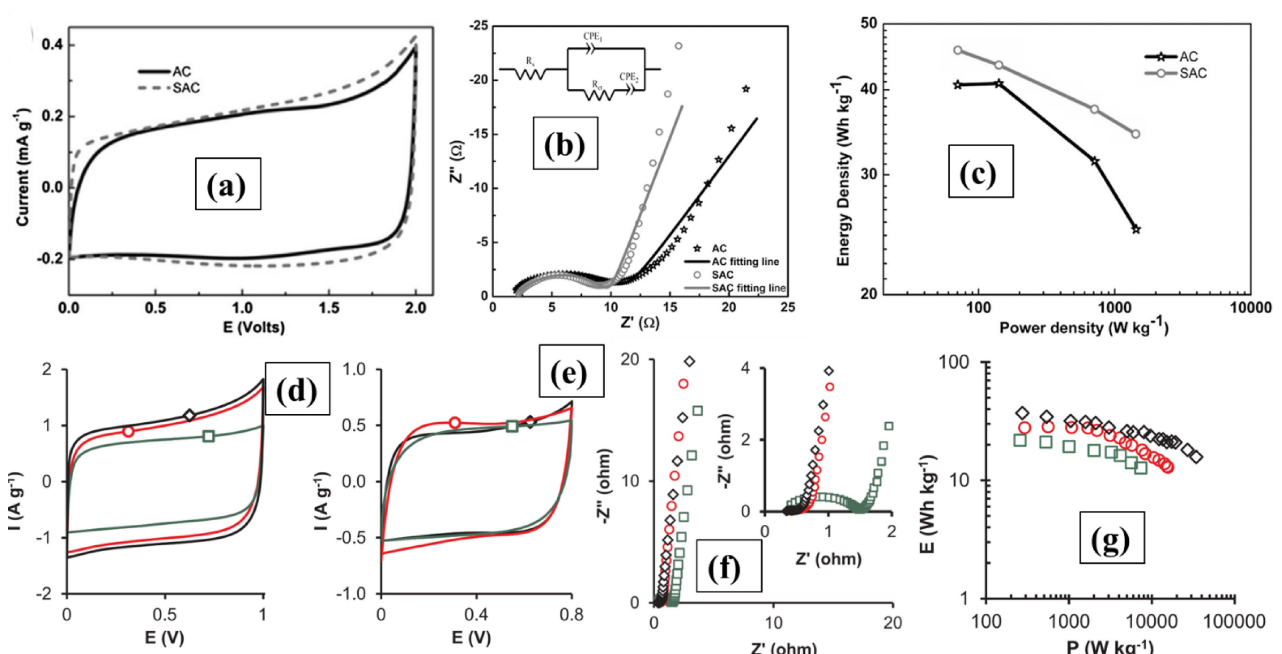


Figure 2. a) CV of AC and SAC (10 mV/s). b) EIS analysis of AC and SAC samples. c) Comparison of Ragone plot depicting the E_s and P_s of AC and SAC, reproduced from ref. [43] Copyright (2014) Elsevier. d) CV curves of AOW, AOW5 and AOW9 in H_2SO_4 1 M. e) CV curves of AOW, AOW5 and AOW9 in KOH 6 M. f) EIS measurement of AOW, AOW5 and AOW9 in H_2SO_4 1 M. g) Ragone plot of AOW, AOW5 and AOW9 in H_2SO_4 1 M, reproduced from ref. [44] Copyright (2018) Elsevier.

values across the given J_s range, signifying improved conductivity.

Elmouwahidi et al. conducted a study in which they employed the conversion of agricultural waste derived from the olive oil industry into activated carbon.^[44] The researchers generated the waste materials through a process that resulted in the formation of Activated Carbon. By carbonizing and chemically activating by-products from the olive oil business, a material with good textural qualities was created. The surface was modified by the introduction of sulfur and oxygen functionalities through a solvothermal treatment with the objective of enhancing their electrochemical performance. The solvothermal process successfully introduced a significant proportion of sulfur and oxygen, primarily located on the external surface of the sample. This modification resulted in functionalized materials with both capacitances (325 versus 158 F/g at 0.125 A/g in H₂SO₄ 1 M). They synthesized activated carbon (AOW), activated carbon weighted 2 g was mixed with 5 ml of thioglycolic acid (AOW5), and Activated carbon weighed 2 g was mixed with 9 ml of thioglycolic acid (AOW9). Cyclic voltammograms at 20 mV/s are displayed in Figure 2(d and e) for all the samples. The utilization of a 6 M potassium hydroxide (KOH) solution as the electrolyte, instead of a 1 M sulphuric acid H₂SO₄ solution, resulted in a decline in the electrochemical performance of the samples. This can be a result of the lower operating potential range of KOHs than H₂SO₄. The Nyquist plots obtained from electrochemical impedance spectroscopy (EIS) data as depicted in Figure 2(f) indicates that all the samples displayed typical feature associated with porous carbon electrode. For AOW, AOW5, and AOW9 the inset depicts the zoom portion of the high frequency area that elaborates the ESR values of 0.41 Ω, 0.38 Ω, and 0.32 Ω respectively. Figure 2(g) illustrates the Ragone plots of the activated carbons (ACs), which portray the upper and lower bounds of power and energy densities within an electrical circuit. The E_s of sample AOW9 reached a peak value of 37.0 Wh/kg, surpassing the average E_s of commercially available Scs (10 Wh/kg). Additionally, AOW, AOW5, and AOW9 each reached a maximum capacitance value of 159 F/g, 246 F/g, and 293 F/g. The suggested solvothermal technique of sulfurization was able to create materials that performed superbly as Sc electrodes, especially in acid electrolytes.

Y. Boyjoo et al. published a research paper discussing the utilization of Coca-Cola as a potential biomass waste material for the synthesis of heteroatom-doped, microporous activated carbon (AC) with a significant area.^[45] These activated carbons were subsequently utilized as absorbents for CO₂ capture and as electrodes for Sc. Dual-doped carbon spheres, incorporating nitrogen (N) and sulfur (S) are synthesized through a hydrothermal process using coca-cola as the precursor material. Subsequently, potassium hydroxide (KOH) or zinc chloride (ZnCl₂) is employed as an activating agent for the thermal activation of the carbon spheres. Four distinct samples, labelled as CMC-1, CMC-2 (ZnCl₂-activated carbon), and CMC-3 (KOH-activated carbon), were prepared. CMC-1 and CMC-2 were synthesized using ZnCl₂/HC mass ratios of 1 and 3, respectively. In contrast, CMC-3 was activated using KOH, with a KOH/HC

mass ratio of 4. To depict a comparative analysis, a sample consisting of non-activated carbon sphere (NACS) obtained through the hydrothermal carbonization process was subjected to calcination without any subsequent activation. In the SEM image for CMC-2 indicates that the particles largely maintain their spherical morphology post-activation yet exhibit signs of erosion and breakage attributed to the corrosive nature of ZnCl₂. The TEM image reveals a significant reduction in particle density due to the development of numerous micropores. In the case of CMC-3 the particle loses their spherical shape, transforming into thin layers that appear peeled. The SEM image of CMC-3 illustrates the formation of flakes and sheets with hierarchically porous surfaces. The thin sheet structure is more evident in the TEM image and HRTEM. The electrode capacitance of the NACS, CMC-1, CMC-2, and CMC-3 samples opted via CV characterization (10 mV/s) as illustrated in Figure 3(a). The presence of carbon-based materials is evidenced by the characteristics of quasi-rectangular formations observed in the CV graphs, which indicates the distinct double-layer capacitance exhibited by these materials. In Figure 3(b), the charged and discharge curves of the carbon electrode at a J_s of 2 A/g are illustrated. The findings suggest that the Cs of the NACS were determined to be 75.1 F/g. According to reports, CMC-1 and CMC-3 contributed Cs of 198.0 and 146.2 F/g, respectively, as shown in Figure 3(c). Among the samples, CMC-2 exhibits the highest capacitance, measuring at 352.7 F/g. The results of this study present encouraging possibilities for the utilization of Coca-Cola and similar soft drinks as effective waste materials or economical substitutes for biomass in the production of high- performance activated carbon (AC). These AC materials can be effectively employed in applications related to environmental remediation, as well as energy storage and conversion. Throughout the hydrothermal carbonization procedure, the inclusion of different additives found in beverages aided in the in-situ introduction of heteroatoms, namely oxygen (O), nitrogen (N), and sulfur (S). Notably, the activation method employed resulted in the formation of two distinct types of activated carbon each exhibiting favorable characteristics suitable for specific applications. One type demonstrated excellent properties as high performance super-capacitors while the other exhibited remarkable attributed as CO₂ adsorbents.

S. Uppugalla and colleagues introduced a novel design for an asymmetrical supercapacitor cell, aimed at achieving a remarkable energy density.^[32] Their design incorporates polyani-line as the positive electrode while the negative electrode consists of activated carbon doped with, specifically nitrogen and sulfur. These electrodes operate within electrolytes composed of aqueous sulfuric acid. Three separate samples were prepared using different amounts of NH₄SCN. The sample prepared with 0.75 g of NH₄SCN was labelled as NSAC-1 the sample with 1.5 g NH₄SCN was labelled NSAC-2 and the sample with 3 g of NH₄SCN was labelled NSAC-3. The same technique was used to produce hydrothermally treated activated carbon (HTAC) utilizing only activated carbon and no NH₄SCN. The hydrothermal method is used to manufacture nitrogen and sulfur-doped activated carbon using ammonium thiocyanate as a precursor heteroatom. The PANI's voltammograms are

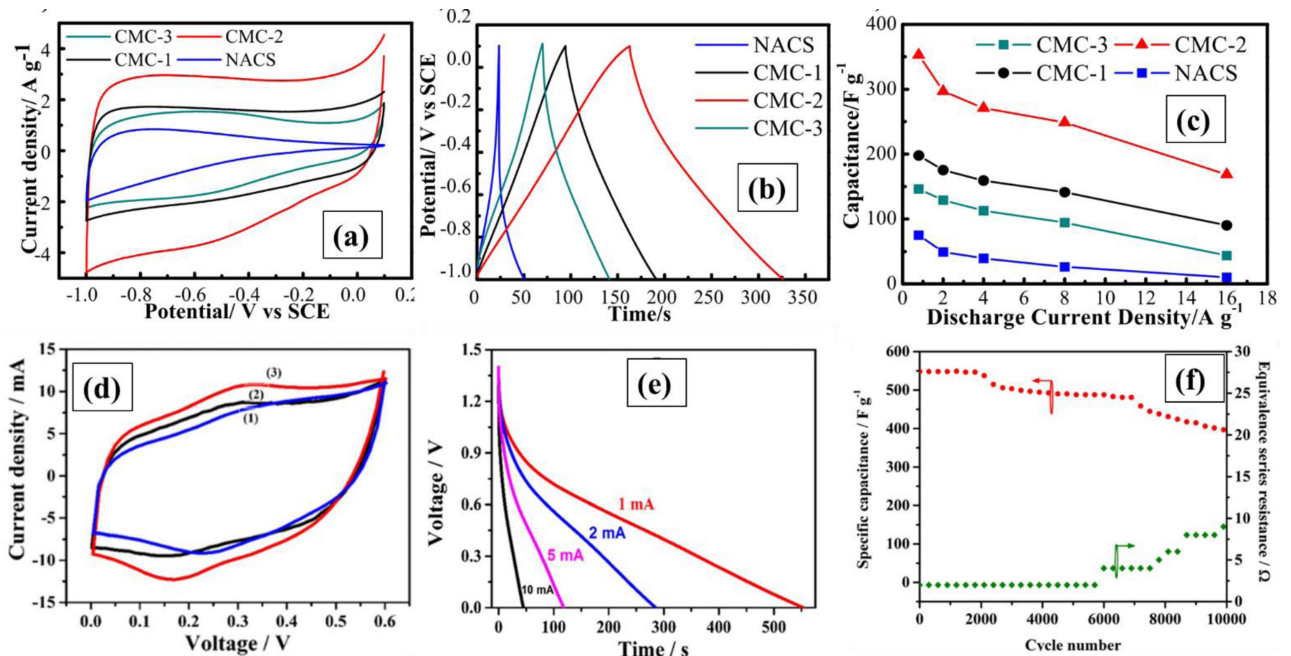


Figure 3. a) CV curves obtained for various carbon materials (10 mV/s). b) GCD curve of carbon materials at 10 A/g. c) Graph illustrating the C_s values calculated from GCD curves, plotted against various current density, reproduced from ref. [45] Copyright (2017) Elsevier. d) CV curves for PANI symmetric cells. e) Depiction of discharge characteristics for aSC across the range of applied currents. f) Evolution of C_s and ESR as a function of cycle number for PANI//NSAC asymmetric supercapacitor aSC measured at a current of 5 mA, reproduced from ref. [32] Copyright (2019) Springer.

displayed in Figure 3(d), where their rectangular form denotes the electrode materials' favorable capacitive behaviour. The discharge curve corresponding to different applied currents (1, 2, 5, and 10 mA) for the galvanostatic charge-discharge (GCD) measurements of PANI/NSAC aSc are depicted in Figure 3(e). By scrutinizing the electrode, the study determined the C_s values of PANI/NSAC at various sulfur contents were found to be 592 F/g, 578 F/g, 548 F/g, and 458 F/g, respectively. The motivation for achieving profitable outcomes is evident from the results obtained through Electrochemical Impedance Spectroscopy. When compared to the previous test, the PANI/NSAC aSc exhibits a significantly lower equivalent resistance (ESR) value of (2Ω). Additionally, to assess the durability of PANI/NSAC and aSc, a consistent CV was conducted using 1 M sulfuric acid (H_2SO_4) electrolytes. The cycling process involved applying a constant current of 5 mA, within the voltage range of 0 to 1.4 V. Figure 3(f) depicts the device's cycling characteristics after 10,000 cycles. The C_s progressively begin to decline after 2000 cycles, and 72% retention shows that the electrodes have high rate capacity cycling performance. The NSAC/PANI aSC asymmetric Sc (aSc) demonstrated favourable electrochemical characteristics, demonstrating a potential window of 1.4 V and E_s of 80 Wh/kg, the system exhibited these characteristics. Following 10,000 charge-discharge cycles, the retained capacitance was determined to be 72% (548 F/g). Notably, the Equivalent Series Resistance (ESR) exhibited a minor increase from 2Ω to 9Ω , indicating a negligible change. The aSC (activated Sc) demonstrated a significantly high phase angle value of 84.6° , closely resembling the phase angle exhibited by an Sc cell under ideal conditions. Moreover, the solution

resistance of the aSC was remarkably low, measuring only 0.12Ω . In order to showcase its functionality, a CR2032 coin cell was employed as a practical demonstration instrument. The commendable electrochemical outcomes, feature E_s of 80 Wh/kg and an operating voltage of 1.4 V with the demonstration of 500 W/kg.

3.1.2. Carbon nanotubes

J. Kim and colleagues conducted a study to examine the electrochemical characteristics of carbon nanotubes dope with sulfur (S-CNTs).^[46] The purpose of their research was to explore the potential benefits of sulfur doping in utilizing S-CNTs as conductive materials in Sc electrodes. In the research conducted by Ji Hoon Kim and his team, they utilized the chemical vapour deposition (CVD) technique to synthesize sulfur-doped carbon nanotubes (S-CNTs), during the CVD process, dimethyl disulfide was employed as the carbon source containing sulfur, Fe/zeolite nanoparticles were utilized as catalyst material. The purpose of this investigation was to assess the electrochemical features of S-CNTs and analyze the effects of sulfur doping on their characteristics. Furthermore, the study sought to explore the suitability of S-CNTs as conductive materials for potential utilization in the fabrication of Sc electrodes. Moreover, a comparative analysis was carried out by the researcher to assess the characteristics of S-CNTs in comparison to commercial multi-walled carbon nanotubes (MWCNTs) and conducting agents referred to as Super-P. To attain purified S-CNTs (denoted as P-S-CNTs), the sample was subjected to a refine-

ment process, resulting in S-CNTs with sulfur contents of 0.65% and diameters ranging from 30 to 50 nm. For the electrochemical evaluation as a supercapacitor electrode FE SEM of S-CNTs were obtained under various synthesis temperatures and H₂ flow rate, with a fixed synthesis duration of 0.5 h. These were subsequently purified to remove residual metallic impurities (P-S-CNTs-100/2). This consistent diameter of S-CNTs after purification and the absence of Fe catalyst at the CNT were confirmed. Figure 4(a) presents at 10 mV/s the CV curves obtained for electrodes prepared using four distinct conducting agents. Symmetrical CV curves were observed for all carbon nanotube specimens, namely P-S-CNTs-100/2, De-P-S-CNTs-100/2, and MWCNTs, indicating comparable electrochemical behaviour. However, the Super-P exhibited a different response compared to the carbon nanotubes. Out of the different electrodes evaluated, the P-S-CNTs-100/2 electrode demonstrated the most distinct rectangular-shaped CV curve, signifying it as the most noteworthy outcome. In Figure 4(b), Nyquist plots depict the EIS outcomes of the electrodes in Scs employing various conducting agents. Within the frequency range of 100 mHz to 1 GHz, the EIS spectrum of all the electrodes exhibited a discernible semicircular pattern in the high-frequency region. The analyzed samples comprised De-P-S-CNTs-100/2 (0.95 Ω), Super-P (1.37 Ω), and MWCNT (0.89 Ω). Among these, the samples P-S-CNTs-100/2 electrode demonstrated the lowest resistance (R) in the electrolytes, exhibiting an ESR value of 0.65 Ω. Figure 4(c) displayed the purified S-CNTs referred to as P-S-CNTs 100/2, as observed in the FE-SEM images. Among the examined electrodes, the utilization of P-S-CNTs demonstrated

the lowest R_{ct} (6.19 Ω). Additionally, the P-S-CNTs electrode exhibited a Cs of 120.2 F/g. In contrast, the Super-P electrode demonstrated a Cs of 8.39 F/g and a charge-transfer resistance of 15–16 Ω. The exceptional outcomes of P-S-CNTs can be caused by improved conductive nature. Significantly, P-S.CNTs-100/2 exhibited the highest capacity preservation, achieving 96%, followed by De-P-S-CNTs-100/2 with 91% and MWCNTs with 88%. This exceptional capacity preservation demonstrates the excellent rate capability. The result anticipates that manipulating the CNT synthesis conditions will allow us to create S-CNTs with improved electrochemical performance.

3.1.3. Carbon fibres

X. Ma et al. provide a detailed explanation of the process employed to generate mesoporous carbon fibers doped with sulfur, attaining a substantial sulfur content of 14.0 atom% (29.4 wt%) through the carbonization of sucrose.^[47] The researchers outline the utilization of porous whiskers that incorporate MgSO₄ as both templates and a sulfur source. Utilizing the MgSO₄-containing whiskers as templates, carbonization of sucrose (1 g) coating on the templates (5 g) produced a fiber-like carbon material labelled as SMC1. TEM and STEM observations revealed a three-dimensional mesoporous structure with pore sizes ranging from 3 to 50 nm in the fibre-like carbon materials. Under ideal circumstances, the attainment of an exceptionally high sulfur (S) concentration at a ratio of 1:5 requires specific conditions. These conditions encompass a

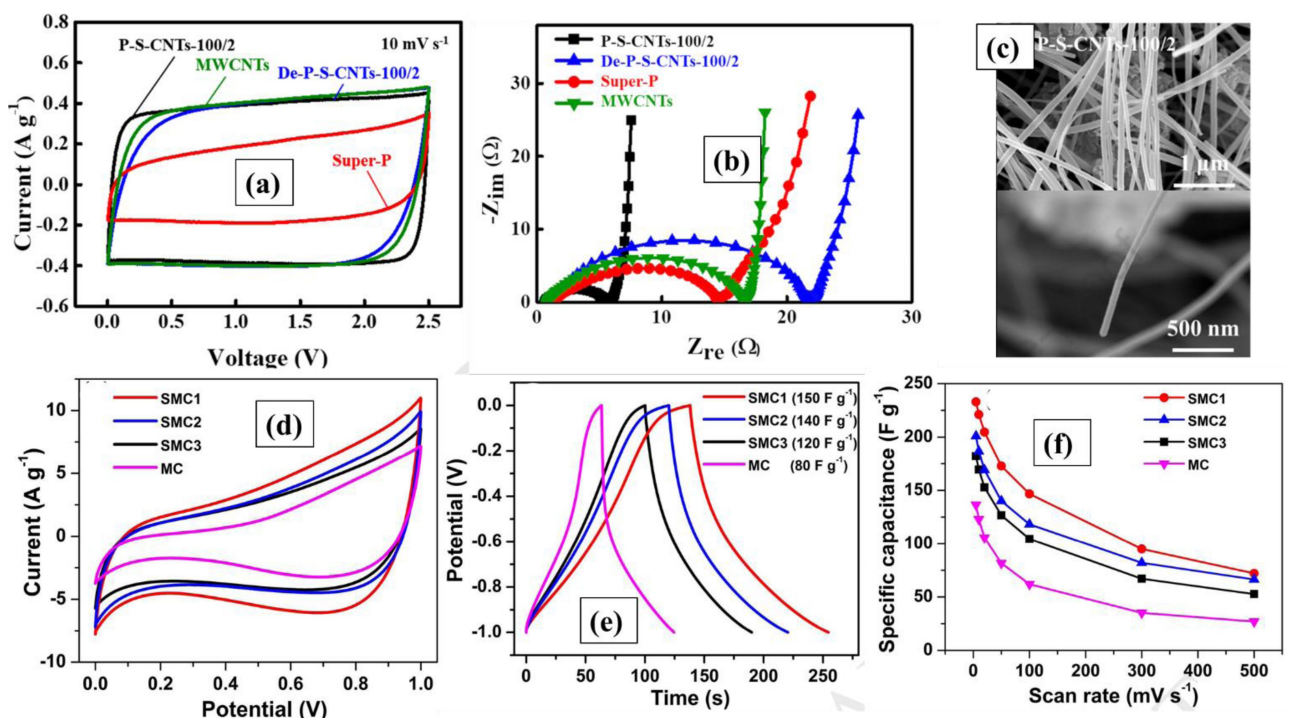


Figure 4. a) Comparison of CV profiles for electrodes containing different conducting agents (10 mV/s). b) Exploring Nyquist plots of supercapacitor electrodes utilizing various conducting agents. c) FE-SEM image depicting P-S-CNTs-100/2, reproduced from ref. [46] Copyright (2021) Elsevier. d) CV curve of porous carbons (50 mV/s) (e) GCD curves of MC and SMCs (1000 mA/g). f) Specific capacitance of MC and SMCs measured at varying scan rates, reproduced from ref. [47] Copyright (2014) Elsevier.

calcination temperature of 600 °C, implementation of whisker templates with reduced diameters, and a significantly lower ratio of carbon supply to templates. Thiophene-S is principally responsible for the bonding configurations of S-(C-S-C), according to X-ray photoelectron spectroscopy. He prepared three samples by the quantity of sucrose, which corresponded to the SMCs designated SMC1, SMC2, and SMC3, which was changed from 1 to 3 g. Comparatively, the same method is used to synthesize undoped MC, but MgO whiskers are used in place of the templates. 513MOS was calcined at 1100 °C to produce the MgO whiskers. Every electrode has a profile that is nearly rectangular in shape and devoid of any discernible redox peaks, as presented in Figure 4(e). The functioning of an ideal double-layer capacitor is shown through the continuous and uniform charge/discharge process of the active materials, maintaining a consistent pace across the complete potential range. With an increasing concentration of S, the Cs of the electrodes exhibit a continuous rise, suggesting that S doping has the potential to greatly enhance Cs. This trend is clearly illustrated in Figure 4(d and e). SMC1 demonstrates a Cs of 221 F/g at a scan rate of 10 mV/s, significantly surpassing the recently published Cs value of S-doped reduced graphene oxide (rGO) (156 F/g). Moreover, the Cs of SMC1 are 1.6 times higher than that of MC, which measures 136 F/g. Figure 4(f) displays the charge/discharge curves of the porous carbons under a constant Js of 1000 mA/g. According to the GDC test, SMC1 has a Cs of 150 F/g, SMC2 of 140 F/g, SMC3 of 120 F/g, and MC of 80 F/g. The rate capability value of SMC1, SMC-2, SMC-3 and MC is 9.61%, 35%, 35.2%, 17.85% at 500 mV/s. A scalable method for producing SMCs with extraordinarily high S concentrations has been developed by X. Ma et al. This approach holds promising potential for the advancement of efficient storage devices.

3.1.4. Porous carbon

In this study, J. Tian et al. fabricated interconnected 3D S-doped porous carbon composites by employing biowaste sodium lignosulfonate as the carbon and sulfur source.^[48] The synthesis process involved direct carbonization followed by a subsequent and further KOH activation step. As a procedure, a vial was utilized to combine 2.0 g of sodium lignosulfonate (LS) and 10 mL DI water. The combination was subjected to stirring for approximately 0.5 hours until complete dissolution was achieved. Subsequently, solutions with varying concentrations of potassium hydroxide (0 wt%, 33 wt%, and 55 wt% with respect to the initial solution) were introduced into the aforementioned mixture and agitated until complete dissolution of potassium hydroxide was achieved. To evaporate deionized water, after being placed in a porcelain boat, the mixture was dried at 110 °C for 10 hours. After undergoing a flushing process with nitrogen gas for a duration of 0.5 hours, the resultant was transferred into a tube furnace and subjected to carbonization at a temperature of 900 °C for a period of 3 hours. The heating rate employed was 5 °C per minute, and the entire process was carried out under the protective atmosphere of nitrogen gas. S-PCs structure analysed with FE-

SEM and FE-TEM, showed S-PC-50 having a 3D honeycomb structure with randomly distributed macropores. The carbonization of sodium lignosulfonates resulted in a highly connected 3D macropore structure. Nitrogen absorption revealed prevalent micropores and mesopores, minimal macropores in S-PC-33 and non in S-PC-0. Potassium compound etching during carbonization created micro/mesopores, while macropores may stem from hydrothermal lignin hydrolysis or structural collapse. EDS elemental mapping of S-PC-50 displayed a homogeneous distribution of C, O, and S, indicating its potential as a superior electrode with a sulfur contribution. Subsequently, the carbon material underwent a series of three rinses using deionized water, continuing until the pH approaches a neutral value of 7. Following the thorough washing procedure, the purified carbon was subjected to a drying process in an oven for a duration of 24 hours at 80 °C. The samples obtained from different potassium hydroxide additions were signified as S-PC-0, S-PC-33, and S-PC-50. Notably, the S-PC-50 sample demonstrated exceptional characteristics, including a significant specific surface area of 1592 m²/g, a notable 5.2 wt% of sulfur (S), and a consistent porous structure composed of macro-, meso-, and micropores. Figure 5(a) exhibits the CV plots of the symmetric Sc with S-PC-50 as the electrode materials. The CV curves were recorded at multiple sweep rates, spanning from 0.005 to 0.800 V/s. Evidently, the CV curves of the S-PC-50 symmetric Sc maintain their rectangular nature even at 800 mV/s, indicating robust electrical double-layer capacitance (EDLC) behaviour and impressive rate performance. Figure 5(b) presents the results obtained from galvanostatic charge-discharge (GCD) measurements, depicting the Cs of the S-PC-50 material. The highest capacitance is significantly higher than carbon-based symmetric Scs at 60 F/g at 0.2 A/g. Figure 5(c) depicts the Ragone plots for the hybrid materials and their corresponding energy performance. The specific hybrid material, denoted as S-PC-50 exhibits an Es of 8.2 Wh/kg at a Ps of 50 W/kg. This performance surpasses the carbon hybrids that were previously reported, specifically rGO, utilized in an aqueous electrolyte. Therefore, the S-PC-50 hybrid demonstrates improved energy characteristics in comparison to existing carbon-based hybrids under similar experimental conditions. At a Js of 0.2 A/g, the maximum Cs recorded was 320 F/g. This result indicates the material's ability to store a significant amount of charge per unit mass under the specified experimental conditions. When measured at a Js of 1 A/g, the S-PC-50 hybrid material exhibits a Cs of 271 F/g. This value is more than twice the Cs of the S-PC-33 hybrid, which is recorded as 132 F/g, and significantly higher than that of the S-PC-0 hybrid, which is measured at 11 F/g. The S-PC-33 hybrid demonstrates a rate capability of 62.5% at 50 A/g and 46% at 100 A/g, while the S-PC-50 hybrid exhibits a rate capability of 20% at 1 A/g. These findings suggest that the S-PC-50 hybrid material possesses superior rate capability compared to S-PC-33 hybrid under the specified conditions. The symmetric Sc comprised of S-PC-50 reveals remarkable cyclic stability and coulombic efficiency, as evidenced by its impressive Es of 8.2 Wh/kg at 50 W/kg.

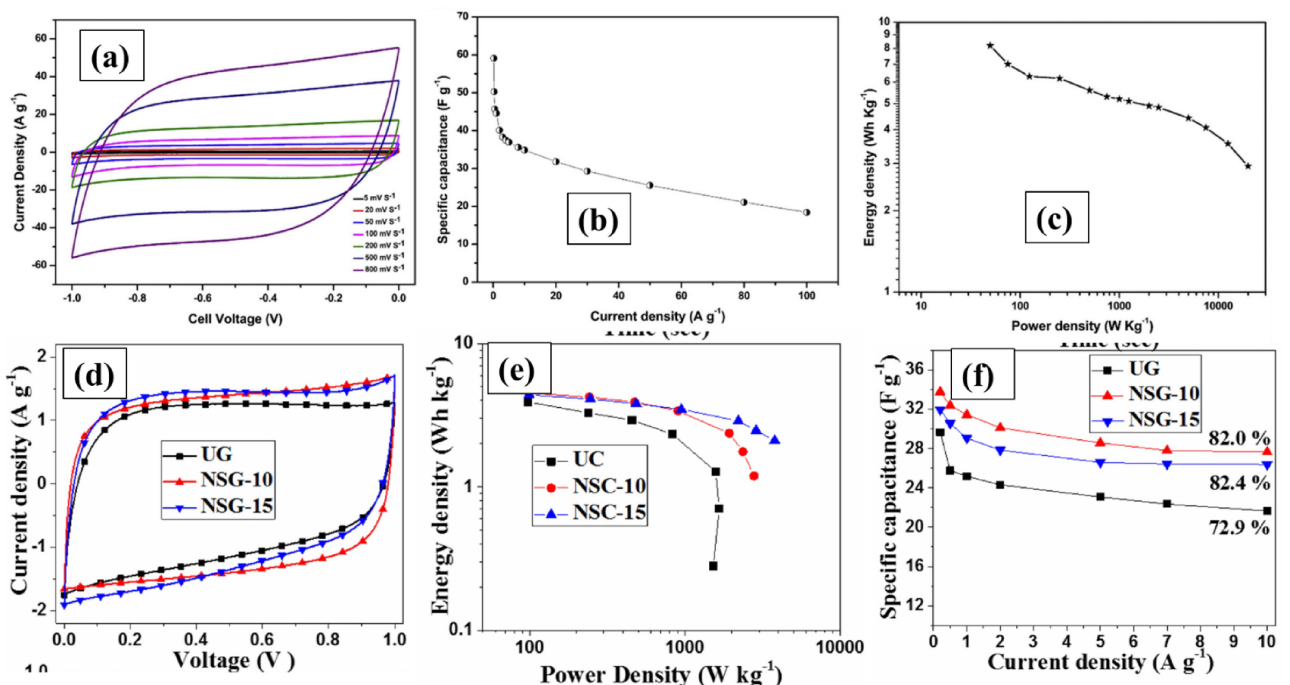


Figure 5. a) S-PC-50 CV. b) Determined Cs through analysis of GCD curve. c) Presentation of Ragone plots for the symmetrical cell employing S-PC-L-900, illustrating the E_s and P_s performance characteristics, reproduced from ref. [48] Copyright (2018) Elsevier. d) Electrochemical characterization of symmetric supercapacitor devices. e) E_s and P_s performance. f) Examining and evaluating rate capacitance for devices, reproduced from ref. [49] Copyright (2019) Springer.

3.1.5. Graphene

Graphene, often referred to as “super carbon” is a nanosheet composed of a single layer of sp^2 -bonded carbon atoms arranged in a two dimensional (2D) honeycomb lattice. In the current study, M. Karuppannan et al. use the mechanical activation approach to successfully synthesize graphene-like carbon sheets that are dual doped with sulfur and nitrogen from coir pith bio-waste.^[49] In the synthesis process, three samples were prepared, to eliminate any residual metal impurities, the co-doped carbon sheets consisting of sulfur and nitrogen, resembling graphene were collected. These sheets were subsequently subjected to agitation in a 1 M HNO_3 solution, followed by thorough rinsing with water to ensure cleanliness. The as-collected sulfur and nitrogen dual-doped graphene were treated with NSG-10, denoting the molar ratio of carbonized coir pith to thiourea. The graphene materials were then dried at 80°C for 12 hours. Additionally, to investigate the impact of sulfur and nitrogen content on capacitance, 6 g of thiourea was introduced to the mixture, resulting in the formation of NSG-15. To assess the impact of co-doping sulfur and nitrogen on carbon sheets resembling graphene, the NSG properties were found contrasted with those of an undoped graphene-like carbon sheet (UG). The UG was synthesized without utilizing thiourea, employing the identical methodology employed for NSG. According to the structural characterization, a carbon network consists of a uniformly doped graphene-like carbon sheet, wherein sulfur and nitrogen atoms are incorporated. The graphene-like carbon sheets co-doped

with nitrogen and sulfur (referred to as NSG) exhibit an amorphous and porous carbon structure that contains flaws. Coir pitch fiber in SEM images undergoes efficient conversion into carbon sheets during UG and NSG-10 processes. SEM verifies nitrogen and sulfur presence in NSG, with elemental compositions of 78.2 wt% 18.5 wt% and 3.2 wt% for carbon nitrogen and sulfur respectively. HR-TEM analysis of NSG-10 shown in HR-TEM reveals the existence of wrinkled and folded graphene-like carbon sheets. A highly magnified view in HR-TEM image reveals the existence of wrinkles and folded graphene-like carbon sheets, and a highly magnified view highlights fringes indicating the partial crystalline nature and porous disorder of graphene-like carbon sheets in NSG-10. These NSG sheets demonstrate a maximum Cs of 247.1 F/g at an applied J_s of 0.2 A/g, and they retain 75.2% of their capacitance when its J_s are increased to 10 A/g. As depicted in Figure 5(d), When the NSG devices were subjected to a scan rate of 50 mV/s, their CV curve exhibited a distinct rectangular shape. This shape indicates the presence of a remarkable double-layer capacitance, along with an increased capacitance attributed to the active sites introduced by heteroatoms. In Figure 5(e), the plots of E_s versus P_s for the UG, NSG-10, and NSG-15 electrodes are illustrated. The values of P_s and E_s were determined by utilizing the Cs of the electrodes at designated J_s . Under the conditions of a J_s of 0.2 A/g, the UG, NSG-10, and NSG-15 electrodes achieved the highest E_s at 3.91, 4.51, and 4.37 Wh/kg, respectively. The NSG-15 device exhibited a significantly high E_s of 4.3 Wh/kg, corresponding to a P_s of 99.24 W/kg. The device demonstrated its peak P_s of 3790 W/kg

while maintaining an E_s of 2.1 Wh/kg. The Cs of the UG, NSG-10, and NSG-15 electrodes were determined to be 133.4 F/g, 204.2 F/g, and 193.8 F/g, respectively, at a Js of 1 A/g. At a Js of 10 A/g, the UG, NSG-10, and NSG-15 electrodes exhibited rate capabilities of 82%, 84.37%, and 73.3%, respectively. Figure 5(f) elucidates the relationship between device capacitance and Js by examining the Galvanostatic Charge-Discharge (GCD) curves obtained from the UG, NSG-10, and NSG-15 devices. The corresponding biomass has emerged as a highly favourable material for energy storage applications. This conclusion is substantiated by the notable durability observed in the NSG device, which remains stable even after undergoing 10,000 cycles.

The recent study conducted by Anuja S. Rajpurohit et al. focuses on bimetallic Cobalt-Nickel tungstate (CoNiWO_4) nanoparticles and their composite with Phosphorous-Sulfur co-doped graphene (P-S-GNS), with emphasis on their hydrothermal synthesis and electrochemical performance.^[50] Various surface and structural characterization techniques were employed to assess the materials, revealing that the bimetallic tungstate particles are securely anchored onto the co-doped graphene surface. SEM analysis was utilized to examine the microstructure of CoNiWO_4 , P-S-GNS, GCE, and $\text{CoNiWO}_4/\text{P-S-GNS}$ nanocomposite. CoNiWO_4 nanoparticles exhibited characteristics slightly spherical morphology with mesoporous features. P-S-GNS revealed entangled graphene-like carbon sheets with significant crumpling induced by heteroatom doping, providing an advantageous structure for CoNiWO_4 adsorption. In the nanocomposite, CoNiWO_4 particles were evenly dispersed on the P-S-GNS, preventing restacking and fostering a loose structure. This promoted accelerated electrolytic ion transport,

enhancing the redox reaction. Importantly, CoNiWO_4 retained its original morphology after integration onto P-S-GNS, emphasizing the effectiveness of graphene sheets in maintaining the nanocomposites structural integrity. In Figure 6(a), the CV curves are depicted for the pure CoNiWO_4 , P-S-GNS, GCE, and $\text{CoNiWO}_4/\text{P-S-GNS}$ composite, allowing for a comparison of their overall electrochemical responses. Remarkably, the $\text{CoNiWO}_4/\text{P-S-GNS}$ exhibits a significantly enhanced electrochemical response, as evidenced by the larger CV curve area, surpassing that of the other electrodes. Figure 6(b) illustrates an equivalent fitting circuit based on Nyquist plots obtained from impedance measurements for the $\text{CoNiWO}_4/\text{P-S-GNS}$, P-S-GNS, and CoNiWO_4 electrodes. Furthermore, Figure 6(c) presents a Ragone plot comparing the constructed device with other well-known Sc devices. The Cs of the $\text{CoNiWO}_4/\text{P-S-GNS}$ at corresponding Js of 0.5, 1, 2, 3, 4, and 5 A/g were measured to be 1298.6, 1254.4, 1135.9, 1075.6, and 1020.7 F/g. CoNiWO_4 exhibited a rate capability of 93.3% at 5 A/g. The fitted R_{ct} value for the hybrid $\text{CoNiWO}_4/\text{P-S-GNS}$ was $1.82\ \Omega$, whereas pure CoNiWO_4 ($4.32\ \Omega$) and P-S-GNS ($5.15\ \Omega$) had higher values. This indicates that the $\text{CoNiWO}_4/\text{P-S-GNS}$ outperforms previously reported materials in the same category. Based on these findings, the study suggests that the $\text{CoNiWO}_4/\text{P-S-GNS}$ holds a promising stake for future energy storage applications.

Sc electrode materials must have a high specific area and involve doping in order to perform properly. Unfortunately, ordinary single doping of materials for two-dimensional electrodes still cannot deliver high supercapacitive performance.^[51] In their study, W. Zhang et al. propose a straightforward hydrothermal technique to synthesize a nitrogen and sulfur co-doped

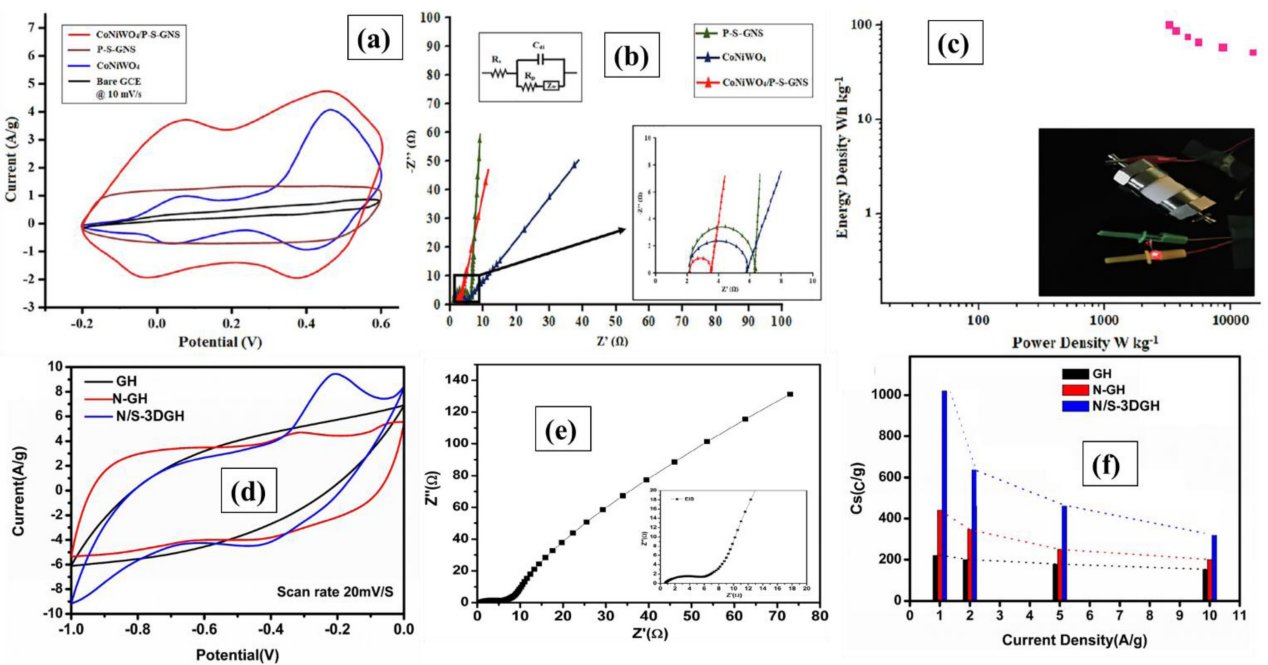


Figure 6. a) Comparative CV curves analysis. b) Impedance-based Nyquist plots, with an inset showcasing the equivalent circuit employed for fitting. c) Ragone plot with inset demonstrates powering the LED, reproduced from ref. [50] Copyright (2019) Elsevier. d) CV (20 mV/s) and e) EIS spectra of hybrid device are presented. f) Cs at various Js. Reproduced from ref. [51] Copyright (2018) Elsevier.

3D graphene hydrogel (N/S-3DGH). This hydrogel serves as an electrode material for Scs and is produced using thiourea as a sulfur source and ammonia as a nitrogen source. He created three samples of graphene hydrogel (GH), one with nitrogen doping (N-GH), one with Nitrogen/Sulfur co-doping (N/S-3DCH), and one without doping at all. The graphene oxide quality significantly influences the performance of the graphene hydrogel. The assessment of graphene oxide quality was conducted through atomic force microscopy (AFM). The AFM image depicts graphene oxides (GO) on the silicon substrate, revealing large sheets with some aggregation. The representative graphene oxide exhibits a thickness of approximately 4.1 nm, equivalent to 6 or 8 layers of graphene oxide. Figure 6(d) displays the CV curves of graphene hydrogels with N-doping and N/S co-doping at 20 mV/s. The GH CV curves' symmetrical and rectangular shape depicts the behaviour of pure double-layer capacitance. The CV curves for N/S-3DGH and N-GH, on the other hand, exhibit peaks at around -0.35 and -0.2 V, respectively, that resemble pseudocapacitance. Figure 6(e) displays the equivalent circuit and EIS spectra for N-GH, N/S-3DGH and GH. A narrow semicircle in the EIS spectrum at high frequency suggests minimal R_{ct} , whereas straight lines at low frequency indicate strong capacitive performance for ASSC. Figure 6(f) displays the calculated average specific capacities of all the samples at various J_s (1–10 A/g). It is obvious that the C_s tend to fall as the J_s rise. In compared to N-GH (210 C/g) and GH (175 C/g) and even at high J_s , the N/S-3DGH has the greatest capacity (389 C/g) respectively. R_s and R_{ct} for GH are $4.7\ \Omega$ and $4.3\ \Omega$, $1.7\ \Omega$ and $4.1\ \Omega$ for N-GH, and $1.42\ \Omega$ and $1.58\ \Omega$ for N/S-3DGH. The rate capability values of N/S-3DGH, N-GH, and GH are 40, 75, and 80%, respectively, with J_s 10 A/g. The findings demonstrate

that the as-prepared N/S-3DGH provides a wide range of extremely intriguing possibilities for portable next-generation energy storage technologies and may greatly improve Sc performance.

In their research, J. Huo et al. utilized a straightforward solvothermal method with the assistance of L-cysteine in ethylene glycol to create sulfur/nitrogen co-doped rGO (SNG) aerogels.^[33] Morphology and composition analyses confirmed the uniform distribution of sulfur/nitrogen (S/N) heteroatoms across the SNG micro sheets, which composed the three-dimensional (3D) porous structure of the SNG aerogels. SEM images reveal the SNG aerogel structure which displays the assembly of SNG sheets and visible inter-sheet holes. Image provides a detailed view of the aerogel, showcasing large SNG sheets forming a porous and interconnected structure. The TEM image depicts micron sized SNG sheets containing C, O, S and N elements. EDX data confirm atomic ratios of 3.54% for S and 2.13% for N elements for N in the SNG aerogel. Elemental mapping in Figures verifies the uniform distribution of C, O, S and N in SNG sheets. The solvothermal preparation method, combined with L-cysteine addition, yields SNG micro sheets constructing a 3D porous structure. The even distributed of S and N in SNG sheets enhances the electrochemical properties of SNG aerogels. Figures 7(a) show the SNG electrode's CV curves over a range of scan rates. The SNG displays evident EDLC characteristics and pseudocapacitance as a result of S/N co-doping, as shown by the fact that these curves are all rectangular in form and devoid of any discernible hillocks. Figure 7(b) displays various J_s GCD curves, together with the EIS spectrum before and after stability. Figure 7(c) displays the triangular-shaped GCD curves of the SNG employing a voltage window of 0 to -1 V. The time needed for charging and

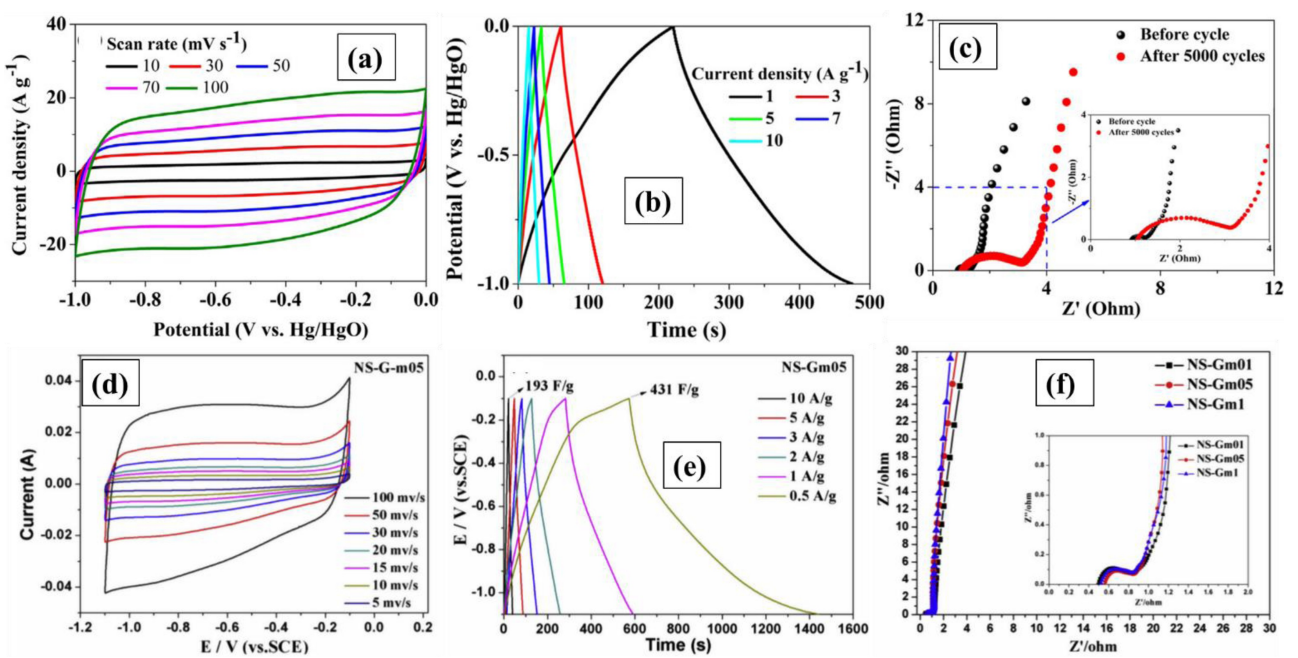


Figure 7. a) CV curve of SNG electrode. b) GCD and c) comparison of EIS curves obtained before cycling and after cycling 5000 cycles, with an enlarged insert showcasing detailed features. Reproduced from ref. [33] Elsevier Copyright (2018). d) CV curve of the NS-G-m05. e) GCD curves of the NS-G-m05. f) Comparative EIS. Reproduced from ref. [52] Copyright (2019) Elsevier.

discharging increases as J_s decline. At J_s of 1, 3, 5, 7, and 10 A/g, the Cs for the SNG electrode are 254, 177.6, 163, 153.3, and 145 F/g, respectively. At 10 A/g, SNG has a particular capability value of 60%. Thus, a method for producing composite composites of SNG with other electrode materials is provided by employing modified SNG with L-cysteine and EG support to create high-performance SC electrodes.

In their study, D. Wu et al. outline a method for synthesizing nitrogen and sulfur co-doped graphene by employing methionine as a doping agent and graphene oxide (GO) as a precursor.^[52] The NS-G hydrogel was freeze-dried for a full night to produce the aerogel NS-Gm05. NS-Gm01 and NS-Gm1 are the names of the produced samples, respectively. In addition to the methionine to GO ratio of 0.5:1, the same synthesis method was used with lower mass ratios of 0.1:1 and higher ratios of 1:1 for comparison. SEM images unveil the microstructure of NS-Gm01, NS-Gm05, and NS-Gm1 aerogels. NS-Gm01 displays closely cross-linked graphene sheets forming a porous network with submicrometric to several micrometre-sized pores. In contrast, NS-Gm05 exhibits a more open 3D structure, indicating enhancing adsorption and ion diffusion capabilities. NS-Gm1 reveals crumpled sheets and tight stacking, signifying notable agglomeration is a consequence of the extensive reduction of GO, leading to negatively charged reduced graphene oxide. XPS analysis validates the significant reduction, diminishing repulsive forces between graphene layers and resulting in aggregation in NS-Gm1. Figure 7(d) depicts the samples' CV curves after they were scanned at various scan speeds for the three samples' voltammograms mostly display an about rectangular form. Figure 7(e) demonstrate the GCD curves, which were determined at J_s ranging from 10 to 0.5 A/g.

For the three samples, the curves that represent the effectiveness of the electric double-layer have nearly triangular forms. Figure 7(f) shows the Nyquist plots for the produced sample data. The three samples' internal resistance is less than 0.6 Ω at high frequencies, demonstrating their low resistance. An incomplete semicircle loop can be seen in the medium-to-high frequency range. For NS-Gm05, the tiniest semicircle has been noticed. As a result, the NS-G has the lowest R_{ct} . At a J_s of 0.5 A/g, the Cs values of the NS-Gm01, NS-Gm05, and NS-Gm1 are 239 F/g, 431 F/g, and 303 F/g.

In a recent study, Delvina Japhet Tarimo et al. reported that the sulfate-rGO (rGO-S) composite was effectively converted into carbon nanorods and fibers using an improved Hummers technique.^[53] The study involved the creation of two types of samples: rGO and rGO-S. SEM analysis discloses unique surface morphologies of the synthesized samples. Reduced graphene oxide (RGO) exhibits a sheets like structure whereas the RGO-S composite showcases a distinctive combination of nanorods and nanofibers resulting from a sulphur-induced chemical reaction. Employing an enhanced Hummers method with sonication and magnetic stirring produces nanorods/nanofibers approximately 150 nm in length, achieving a homogeneous blend of reactants. The introduction of sulfur, coupled with continuous stirring and sonication without the need for hydrothermal or reflux setups facilitates nanorods/fibers growth initiated by sulfur-active sites. This morphology, evident in SEM images is substantiated by TEM micrographs for both RGO and RGO-S samples. In Figure 8(a), the CV curves are presented for both samples, exhibiting pseudocapacitive behaviour in the negative potential window and Faradaic activity in the positive potential window. Figure 8(b) illustrates the GCD curves for the

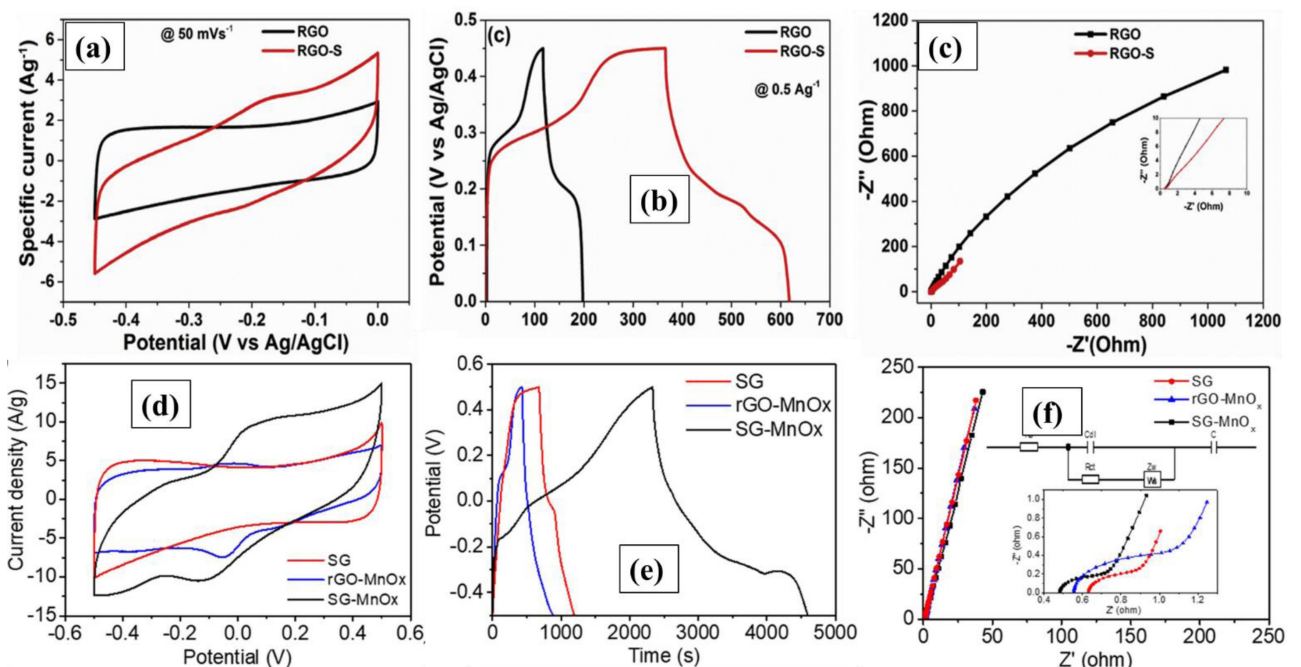


Figure 8. a) CV curves (50 mV/s) within negative potential windows. b) GCD curves and c) Nyquist plots of EIS measurements. Reproduced from ref. [53] Copyright (2020) Elsevier. d) CV curves (50 mV/s), e) comparative GCD and f) Nyquist plot illustrating the EIS characteristics. Reproduced from ref. [54] Copyright (2020) Elsevier.

RGO and RGO-S samples in 6 M KOH at a J_s of 0.5 A/g, separately showing their behaviour in the positive and negative operating potential ranges. Additionally, Figure 8(c) displays the Nyquist plots obtained from electrochemical impedance spectroscopy (EIS) for the RGO and RGO-S samples in 6 M KOH. The EIS Nquist graphs in Figure 8(c) illustrate the frequency response characteristics of RGO and RGO-S with respect to an AC impedance spectrum. At a particular current of 0.5 A/g, the highest values of the RGO and RGO-S electrodes were 12.5 mAh/g and 113.8 mAh/g, respectively. RGO-S has a low equivalent ESR rating of 0.43 Ω compared to RGO's 0.65 Ω . The rate capability values of RGO-S and RGO are 40%, and 20% at 20 A/g. The manufactured sample showed excellent electrochemical characteristics, indicating that the materials might be used in Scs.

According to Q. Lv et al. sulfidation is the most promising technique for creating an electron-dense active region on the surface of materials based on graphene.^[54] The work established an ecologically acceptable approach for the production of sulfur-doped graphene (SG) and mixed-valent manganese oxides (MnO_x). SEM and TEM were employed to examine the morphology and microstructure of SG and SG- MnO_x . High-magnification FE-SEM images of SG reveal a distinctive wrinkle sheet, characteristics of a three-dimensional graphene-based structure. The surface of SG- MnO_x is uniformly coated with flower-like MnO_x nanosheets. These thin nanosheets offer larger volumes and available areas, enhancing electron storage for improved capacitive performance. The flower-like structure also increases contact areas between the electrolytes and active materials, facilitating the reversible redox reactions. SG, rGO mixed-valent manganese oxides (rGO- MnO_x), and SG-mixed-valent manganese oxides (SG- MnO_x) CVs are compared in Figure 8(d), while the GCD profiles of these materials at 0.5 A/g are contrasted in Figure 8(e). Figure 8(d) displays the CV curves for all the fabricated electrodes. In SG- MnO_x , there are unmistakable redox peaks at positions of roughly -0.136 and 0.043 V, respectively. These peaks are caused by reversible Faradaic redox processes. Figure 8(e) depicts the GCD curves for the three samples. In comparison to SG and rGO- MnO_x electrodes, SG- MnO_x electrodes exhibit substantially longer discharge durations, which suggests significantly greater Cs. According to calculations, the CS of SG- MnO_x is 1131 F/g, greater than the rGO- MnO_x (227 F/g) and SG (255 F/g) at 0.5 A/g. Further testing of the EIS was done to corroborate the finding shown in Figure 8(f) (Nyquist plot). With R_s , R_{ct} , C_{dl} , and Z_w standing for the electrolyte solution resistance, R_{ct} , capacitance, and Warburg impedance, an analogous circuit was developed to replicate EIS data. In addition to providing a simple, safe, and environmentally sound synthetic approach, the findings of this work may be applied to various metal oxide composite heteroatom-doped graphene materials.

L. Cheng et al. A novel, the speedy, one-step method based on an electron beam (EB) was successfully employed to produce N, S-codoped graphene layers (NSG) and reduce graphene oxide (GO).^[55] A highly reducing species must be created in order to reduce the graphene oxide to rGO and dope sulfur and nitrogen into graphene. For this synthesis to take place, high-

energy electron beam rays must interact with water that includes L-cysteine, which is the precursor to sulfur and nitrogen. TEM and SEM with EDX were employed to scrutinize the morphology and structure of pristine GO and NSGs. The TEM image of NSG-210 reveals a wrinkled morphology with multiple stacked layers, in contrast to the relatively smooth surface of pristine GO (SEM). Elemental mapping of C, O, S, and N for NSG-210 clearly shows a homogenous distribution of doped N and S atoms across the entire plane, confirming the successful fabrication of NSGs. Figure 9(a) displays the comparable cyclic voltammograms of RGO-350 and NSGs, which were generated at 50 mV/s inside an operating window of 0 to -1.00 V versus Hg/HgO. The NSGs and RGO-350 CV curves at 50 mV/s. The inset displays the similar circuit that was used to fit the resultant Nyquist plots. The EIS data from the NSG samples and undoped RGO-350 were further examined using Nyquist plots, as seen in Figure 9(b). The simple equivalent circuit shown in the inset may be utilized fit the EIS spectrum. Figure 9(c) Ragone's plot of the specific power of the NSG vs its Es using a two-electrode cell. At 510 W/kg of Ps, the NSG-210 Sc can supply 8.3 Wh/kg of energy, according to the Ragone plot. At a greater Ps of 10440 W/kg, 5.8 Wh/kg of energy may be stored. A high J_s of 20.0 A/g may be handled by the NSG-210//NSG-210 symmetric Sc device while still preserving a Cs of 41.7 F/g. In contrast, the device using electrodes from the NSG-70, NSG-140, and NSG-350 exhibits much lower Cs values (41.3 F/g for the NSG-70, 55.1 F/g for the NSG-140, and 28.1 F/g for the NSG-350 at 1 A/g). The radiation doses for these four suspensions were 70, 140, 210, and 280 kGy, and the samples were placed in the radiation field around 30 cm from the radiation source. Centrifugal separation was used to separate the products, multiple washes in ethanol and DI water, and vacuum freeze drying before being dried. The NSG-irradiation doses of the samples, such as NSG-70, NSG-140, NSG-210, and NSG-350, were used to identify them. At high frequencies, it was discovered that the equivalent ESR of the NSG-70, NSG-140, NSG-210, and NSG-350 was 0.65 Ω , 0.64 Ω , 0.64 Ω , and 0.66 Ω , respectively. NSG-70, NSG-10, NSG-210, and NSG-350 have rate capability values of 75%, 60%, 83%, and 83% at 20 A/g, respectively. According to research by Lingli Cheng and colleagues, a variety of graphene-based materials that are heteroatom- or co-doped may be created and manufactured on a massive scale, putting up suggestions for possible use of these materials in sensors, fuel cells, and other energy storage devices.

The two-dimensional lamellar structure of graphene makes it a promising material for Sc. Unfortunately, their electrochemical profits are well below the expected (theoretical). Y. Chen et al. present rGO aerogels (N/S-rGAs), made by using a one-pot hydrothermal technique with trithiocyanuric acid as a doping agent.^[56] These aerogels were co-doped with various concentrations of sulfur and nitrogen. SEM and TEM analysis were employed to investigate the microstructural characteristics of undoped reduced graphene oxide aerogel (rGA) and N/S-rGas. The SEM image of rGA displays a porous block structure formed through the overlap and agglomeration of graphene sheets. In contrast, N/S-rGA-1 exhibits a continuous cotton-like

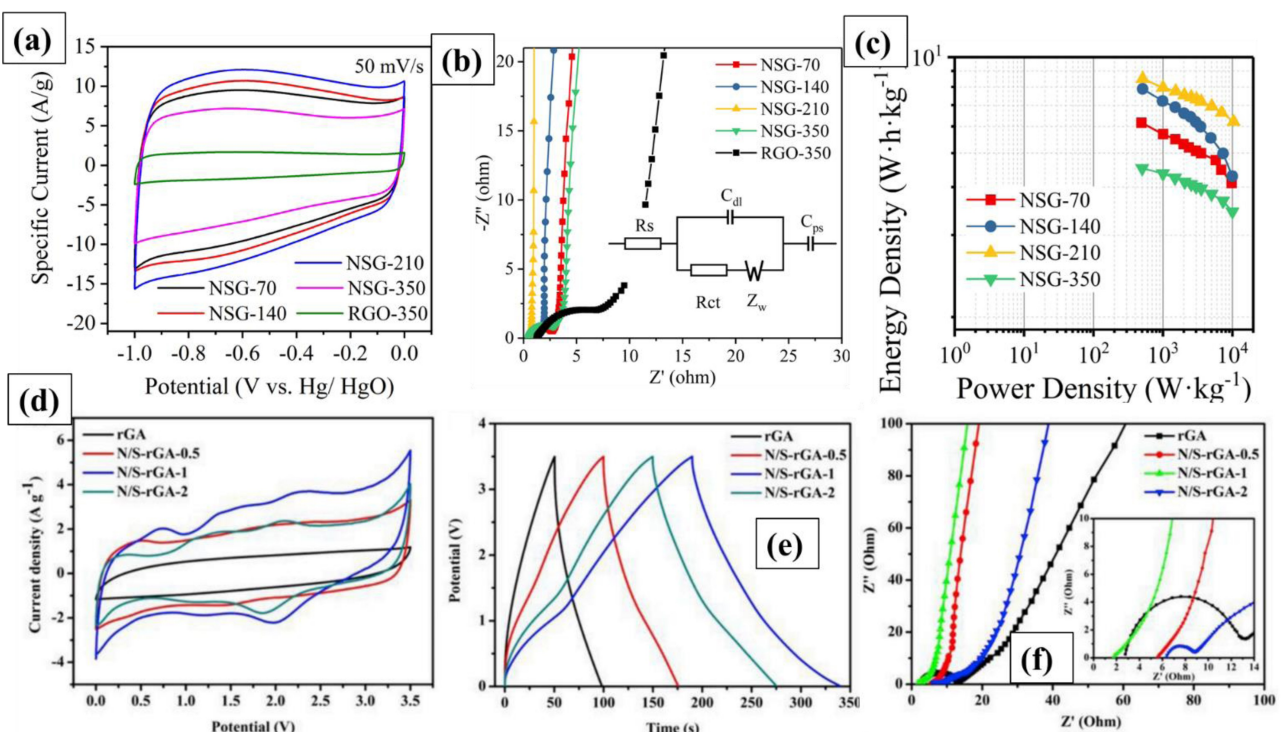


Figure 9. a) CV (50 mV/s) and b) Nyquist plots depicting the characteristics of NSG and undoped RGO-350, accompanied by an inset illustrating the corresponding fitted circuit. c) Ragone plot illustrating the relationship between P_s and E_s . Reproduced from ref. [55] Copyright (2018) Elsevier. d) CV curves (20 mV/s), e) GCD (2 A/g) and f) Nyquist plots displaying the impedance characteristics. Reproduced from ref. [56] Copyright (2019) Elsevier.

porous structure with good uniformity. The TEM images of rGA reveal an opaque sheet while N/S-rGA-1 exhibits a thin, crumpled texture without severe aggregation. The distinct morphology of N/S-rGA-1 resulting from the addition of heteroatoms into graphene lattice, provides more adsorption sites and transmission channels, improving accessibility for electrolyte ions. The interconnected porous structure is believed to enhance energy storage, leading to improved electrochemical properties. SEM and TEM images of N/S-rGA-0.5 and N/S-rGA-2 indicate porous structure Albert with uneven morphologies due to agglomeration and collapse of graphene layers. The CV curves, recorded at 20 mV/s, are shown in Figure 9(d). The rGA CV curve's symmetrical, almost rectangular form indicates pure electrochemical double-layer capacitance behaviour. N/S-rGAs' CV curves are similarly rectangular, which suggests that electrical double-layer capacitance serves as the material's main energy storage mechanism. The GCD curves examined at a J_s of 2 A/g revealed almost symmetrical triangular shapes, which supports optimal capacitor behaviour as shown in Figure 9(e). The C_s of N/S-rGA-1 was estimated from its discharge curve to be 175.8 F/g at 2 A/g in contrast to rGA (53.7 F/g), N/S-rGA-2 (147.3 F/g), and N/S-rGA-0.5 (135.2 F/g). The symmetric Scs' Nyquist charts are shown in Figure 9(f). The plots' x-axis intercept was reported to be caused by the combined resistance (R_s). Both the internal resistance, along with the contact resistance between the separator and active material, influence the overall performance of the system. N/S-rGA-1 had the lowest R_s among the materials, with values of 2.78 Ω ,

5.59 Ω , 1.72 Ω , and 6.42 Ω for rGA, N/S-rGA-0.5, and N/S-rGA-1 and N/S-rGA, respectively. N/S-rGA-1, N/S-rGA-2, N/S-rGA-0.5, and rGA have respective rate capacity values of 85, 80, 66, and 33% at 10 A/g. High-performance Sc is now feasible due to the superior electrochemical outcomes of N/S-rGA-1.

According to X. Zhang et al., one of the best ways to further improve the supercapacitive characteristics of carbon materials is by heteroatom doping.^[57] Most studies to far have concentrated on the impact of the type and quantity of doping agents. By reducing graphene with urea, S-RGO, or sulfur-doped graphene, was created. Briefly, 60 mL of deionized water was combined with 0.1 g of S-GO, and the mixture was ultrasonically dispersed for 30 minutes. The mixture was next placed in a 100 cc Teflon autoclave and hydrothermally treated for 12 hours at 180 °C after receiving 0.5 g of urea and an additional 30 minutes of magnetic stirring. The resultant solid samples were filtered, then dried for 10 hours at 80 °C to create S-RGOs (marked as S-RGO-200, S-RGO-400, S-RGO-600, S-RGO-800, and S-RGO-1000, respectively). TEM images depict undoped RGO and S-RGO samples. Both samples exhibit semi-transparent features in the electron beam. Undoped RGO sheets appear smoother and exhibit significant self-stacking, while S-RGO sheets display wrinkles and folds. The observed morphology difference is attributed to sulfur doping in the graphene nanosheets. Heteroatom doping induces an increase in bond length and a decrease in bond angles, leading to the formation of wrinkles in graphene. The performances were assessed using 6 M KOH, as illustrated in Figure 10(a). By calculating the

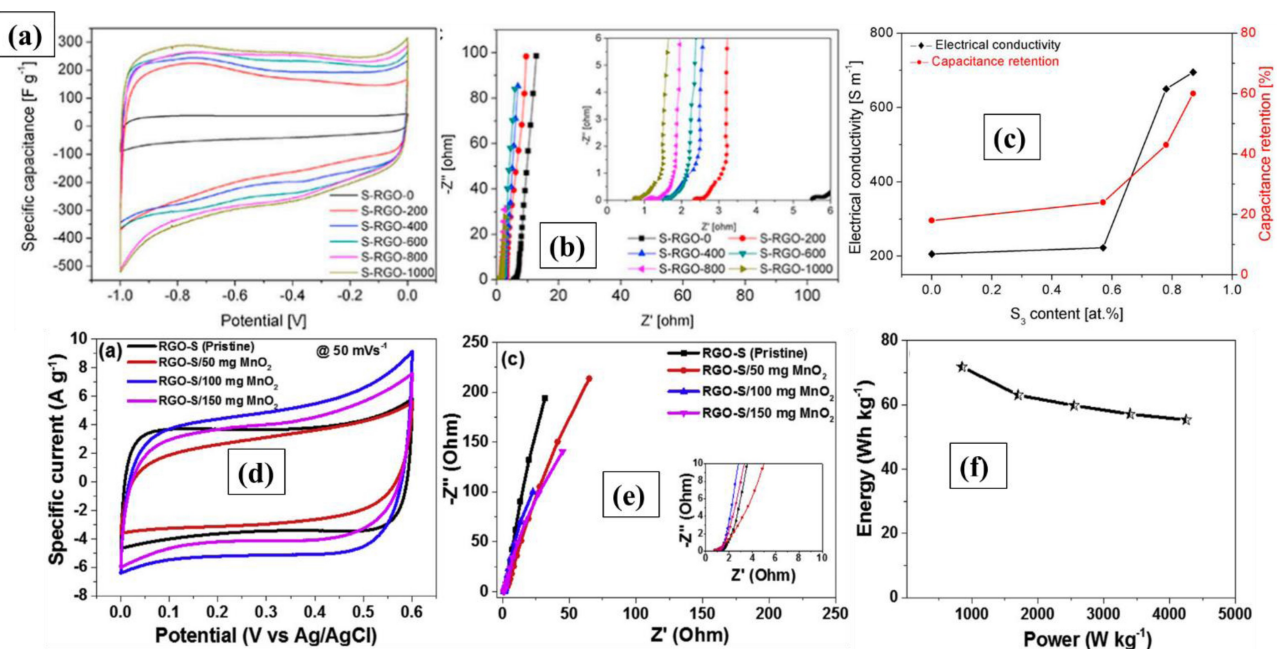


Figure 10. a) The CV plots of S-RGOs at 50 mV/s. b) The Nyquist plots of S-RGOs is presented, accompanied by an inset highlighting the high frequency segment for detailed analysis. c) The electrical conductivity dependence on performance. Reproduced from ref. [57] Copyright (2019) Elsevier. d) CV curves within positive potential window. e) The EIS Nyquist plots illustrates the variation observed in RGOs/MnO₂ with different MnO₂ loadings, using a 2.5 M KNO₃ electrolyte. f) The Ragone plot illustrating the performance evaluation of a system in a 2.5 M KOH₃ electrolyte. Reproduced from ref. [58] Copyright (2020) Elsevier.

integrated area of the cyclic voltammogram (CV), the capacitance values (C_s) for S-RGO-0, S-RGO-200, S-RGO-400, S-RGO-600, S-RGO-800, and S-RGO-1000 at 5 mV/s are determined to be 40.0, 181.5, 209.3, 237.0, 253.2, and 270.4 F/g, respectively, indicating a noticeably improved capacitive performance brought on by the S-doping. In comparison to the undoped RGO, every sample of S-RGO exhibits a much decreased equivalent ESR Figure 10(b). This improved cyclic potential can be seen in the EIS of S-RGOs (Nyquist plots) before and after 10,000 cycles. The electrical conductivity comparable to temperature dependences are shown in Figure 10(c), the S₃ species may contribute more to the electrical conductivity of the S-doped graphene. The rate capability S-RGO-100, S-RGO-800, At 500 mV/s, S-RGO-600, S-RGO-400, S-RGO-200, and S-RGO-0 are respectively 61, 64, 28, 25, 23, and 25%. This study effectively demonstrates a method to improve the supercapacitive performance Based on heteroatoms-doped materials.

Delvin Japhet Tarimo et al. successfully employed rGO-S and rGO-S oxide/manganese dioxide (RGO-S/MnO₂) composites to construct nanorods/fibers, nanosheets, and nano-flower-like structures for use in Sc applications.^[58] According to structural, chemical composition, and morphological examinations, the RGO-S/MnO₂ and RGO-S were synthesized. The morphology and composition of synthesized RGO-S and its composites are analyzed through SEM. The SEM images of RGO-S confirm the formation of nanorods/nanofibers and nanosheets attributed to sulfur and ascorbic acid. SEM images of RGO-S/MnO₂ composites with varying MnO₂ masses and TEM micrographs demonstrate composite structures. RGO-S/100 mg MnO₂ exhibits a porous structure, enhancing electrolyte ion passage compared

to other masses. EDX analysis confirms elemental composition in RGO-S, MnO₂ and RGO-S/MnO₂ composites, with observed K resulting from KMnO₄ used in synthesis. The Nyquist curve from the EIS test performed on the device before and after the stability test is shown in Figure 10(d). The small semicircle in a high frequency region that was observed is proof of good ion diffusion and low resistance, which assisted in explaining the enhanced capacitive behaviour of Sc. At scan speeds of 50 mV/s rectangular CV curves of all the samples are presented in Figure 10(e). The absence of redox peaks and rectangular overall CV curves indicate that EDLC predominates in the materials. After being liquefied in 80 mL of DI water, 1 g of RGO-S was added to a solution. Adding 50 mg of MnO₂ that had been produced for one hour, the solution was then stirred for five minutes. The processes were repeated with 100 mg and 150 mg of MnO₂ synthesized for 1 hour. The suspension was put into the autoclave and cooked for one hour at 150 °C in the oven. After the solution had reached room temperature, it was periodically washed with DI water before being dried for 12 hours in the oven. The device was found to have an E_s of around 71.74 Wh/kg and a specific power of 850 W/kg according to the so-called Ragone plot (E_s versus specific power plot), which is seen in Figure 10(f) marking their potential for exceptional applications.

The creation of S-doped graphene oxide hybrid nanosheets using in situ polymerization was demonstrated by Akram Alabadi et al.^[59] The examination of morphology through (FE-SEM) for G-TB demonstrated the evolution of stacked sheets into a cohesive and thick graphene structure, attributed to the presence of the PTCB film. In contrast, the GO-TB sample

displayed noticeable pores and wrinkles at the edges, contributing to an increased crumpling of ions onto the electrode surface. High-resolution transmission electron microscopy (HR-TEM) findings indicated that the G-TB sample formed a substantial and thick two-dimensional structure, while the GO-TB sample exhibited fewer layers. This thorough synthetic approach and morphological assessment offer valuable insights into the distinctive structural features of the composite's materials. According to the charge/discharge curve in three electrode systems, it works well as an electroactive material in an alkali aqueous electrolyte and has a high Cs (up to 296 F/g) at a Js of 0.3 A/g. The poly[(Thiophene-2,5-diyl)-co-(benzylidene)] (GO-TB) electrode's CV curves all have the characteristic rectangular shape even at high scan rates, as illustrated in Figure 11(a), indicating that it has a higher Cs and a lower ESR. At low discharge Js, the GO-TB electrode's Cs is higher than the G-TB electrode's. The maximal Cs of G-TB and GO-TB are therefore 217 F/g and 296 F/g, respectively, with a Js of 0.3 A/g. At a high Js of 30.2 A/g, the GO-TB's high rate capability is also shown, and the capacitance can sustain a value of around 69% of its maximum Figure 11(b). GO-TB composite clearly performs PANI-GO (220 F/g, 84%), PANI-rGO (259 F/g, 81%), and PPy/MGO (202 F/g, 83.8%) in terms of capacitance and cyclic life. GO-TB composite is also more durable. The Nyquist plots provide more evidence of GO-superior TB's conductivity as shown in Figure 11(c). The GO-TB semicircle (Rs) is smaller (nearly vertical) in the low frequency area leads one to believe that the GO-TB electrode cell has a lower ESR, a crucial sign of the speed at which ions. GO-TB and G-TB have a rate capability of 75 and 44%, respectively, at 30 A/g. Composites made of conducting polymers and GO have

promise for use as energy storage systems' electrode materials. A straightforward, one-step green manufacturing process that employs ammonium thiocyanate (NH_4SCN) as the single source of both nitrogen and sulfur and no extra alkali sources or dispersants has been used to effectively produce N- Fe_2O_3 /NSG composite.^[60]

Unexpectedly, the hydrothermal mechanism accumulates N atoms into graphene while also doping them into Fe_2O_3 . From the SEM image the GO morphology resembles a silk mask, typical of GO reduction. SEM highlights more prominent wrinkles on nitrogen-doped graphene (NSG), attributed to heteroatom-induced structural defects, hindering material aggregation and aiding N- Fe_2O_3 nanoparticle attachment during hydrothermal growth. In SEM image of N-Fe203/NSG, small N- Fe_2O_3 nanoparticles are not distinctly visible. However, the TEM image confirms uniform distribution on NSG, with an average diameter of 20–30 nm. This examination provides concise insight into N- Fe_2O_3 /NSG morphology, clarifying the impact of heteroatom doping and hydrothermal growth on the structure of the material. The Fe_2O_3 and N- Fe_2O_3 electrode CV curves in Figure 11(d) were seen to be somewhat distorted at a scanning rate of 10 mV/s. There are two separate redox peaks evident on the CV graph. For Js of 1, 2, 3, 5, and 10 A/g, N- Fe_2O_3 /NSG possesses Cs of 1567, 1534, 1438, 1240, and 864 F/g, respectively. N- Fe_2O_3 and N- Fe_2O_3 /NSG composite have Rs and R_{ct} values of 1.35 Ω, 4.89 Ω and 0.73 Ω, 2.97 Ω, respectively, as illustrated in Figure 11(e). N- Fe_2O_3 /NSG composite has a lower internal resistance in the high frequency region compared to N- Fe_2O_3 and a wider slope in the low frequency region, which suggests a higher electron conductivity. According to the Ragone plot in Figure 11(f), the N- Fe_2O_3 /NSG/AC ASC

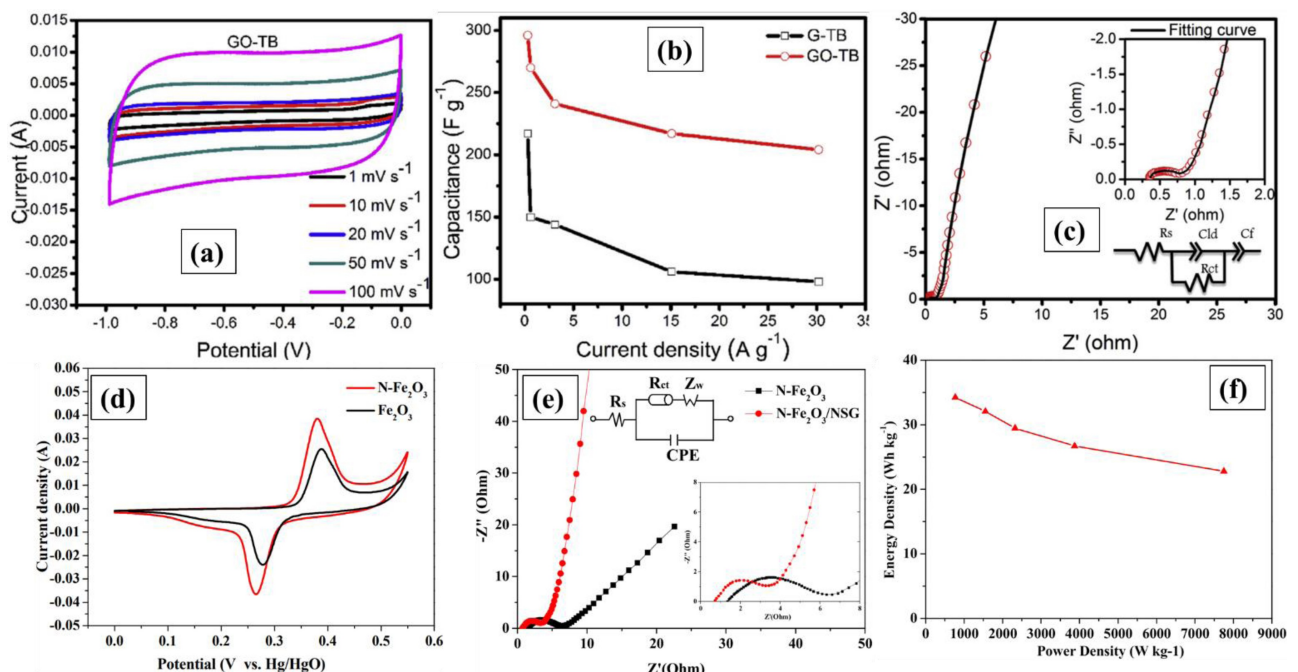


Figure 11. a) CV, b) the Cs retention and c) EIS along with fitted outcomes, reproduced from ref. [59] Copyright (2016) Elsevier. d) Comparative CV curves of Fe_2O_3 and N- Fe_2O_3 electrodes (10 mV/s). e) The EIS of N- Fe_2O_3 and N- Fe_2O_3 /NSG composite. f) The Ragone plot illustrating the Es and Ps performance of the N- Fe_2O_3 /NSG//AC ASC (Asymmetric Supercapacitor) system. Reproduced from ref. [60] Copyright (2018) Elsevier.

generates a high E_s of 34.2 Wh/kg at P_s of 775 W/kg and 22.8 Wh/kg at 7.7 kW/kg. N–Fe₂O₃/NSG has a rated capacity of 62.5%. N, S dual-doped graphene (NSG) is 75% and N–Fe₂O₃ is 62.5%, whereas graphite oxide (GO) is 58.8% at 10 A/g. According to Ying Wang, Mingmei Zhang, and others, the N–Fe₂O₃/NSG composite makes a strong option for an effective next generation optimal Sc application.^[60]

3.2. Sulfidation of MOFs/MOFs derived materials

Metal-organic frameworks (MOFs) possess a unique structure and high porosity, making them an ideal platform for the creation of electroactive materials in electrochemical energy storage applications. However, designing multi-component electrode materials with enhanced performance for Scs by fully utilizing the structural advantages of MOFs remains a challenge. In a recent study, carbon-coated spherical sulfide nanostructures were synthesized through simultaneous sulfurization and carbonization, using bimetallic or monometallic MOFs as precursor materials.^[61] The samples obtained in this study were subjected to annealing in a tube furnace using a CS₂/N₂

atmosphere. The CS₂ gas was removed from the system by N₂ gas flowing in a specific direction (as illustrated in Figure 12a) to facilitate the sulfurization of the samples. The annealing process was carried out at a temperature of 500 °C for 2 hours (5 °C per minute heating rate) and 100 ml per minute (flow rate). These conditions ensured that the samples underwent both complete sulfurization and carbonization. The preparation of NiCo–MOF solid spheres was achieved with diameters ranging from 3–4 μm. After undergoing carbonization and sulfurization, the resulting structure maintained its spherical shape similar to the NiCo–MOF precursor. Nevertheless, at the microscopic level, the spheres transformed NiCo₂S₄@C nanoparticles, exhibiting a textured surface as depicted in Figure 12(b). The composite nanoparticles obtained, namely NiCo₂S₄@C and NiS@C, displayed remarkable characteristics including excellent conductivity, substantial porosity, and elevated reactivity. Particularly, the NiCo₂S₄@C composite-based electrode exhibited a significant specific capacity of 948.9 C/g. Furthermore, a hybrid Sc system was constructed by combining NiCo₂S₄@C (positive) and AC (negative) as depicted in Figure 12(c). This configuration yielded an E_s of 43.8 Wh/kg at a P_s of 799.1 W/kg, along with 81.9% retention (5000 cycles). These

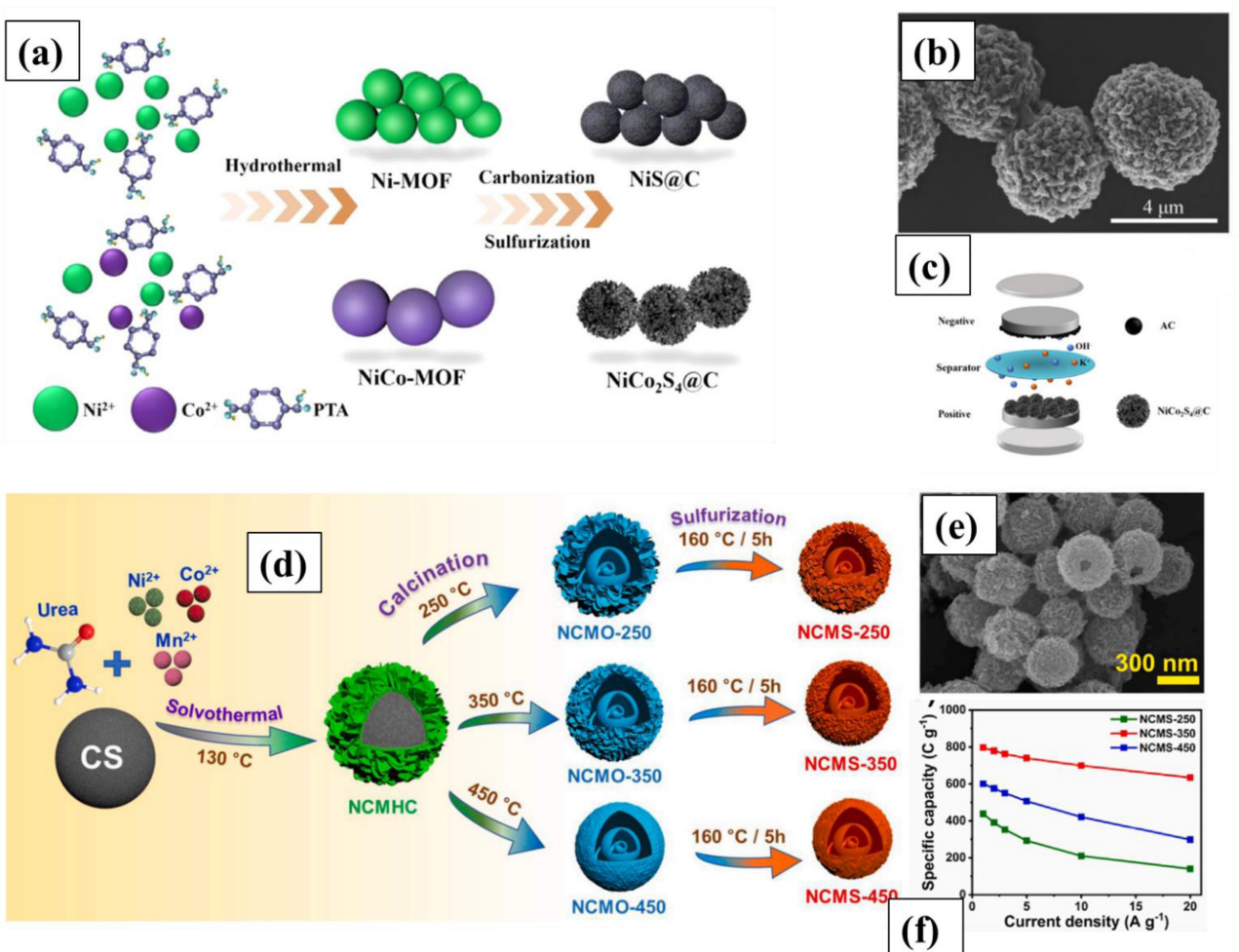


Figure 12. a) Synthetic illustration, b) SEM and c) real device schematic. Reproduced from ref. [61] Copyright (2023) Elsevier. d) Sulfidation process, e) SEM and f) specific capacity trend for multiple samples. Reproduced from ref. [63] Copyright (2023) Elsevier.

findings provide compelling evidence for the viability of utilizing MOFs as precursors for synthesizing advanced multi-component materials based on sulfides, enabling enhanced electrochemical energy storage capabilities.

Q. Liu and co-workers successfully synthesized hollow rod-like nanosheets of NiCoMn ternary metal sulfides derived from MOFs.^[62] The synthesis process involved etching/ion-exchange reactions and additional sulfurization. The resulting hollow structure architecture proved advantageous for electrolyte penetration and electron/ion transportation and exhibited remarkable electrochemical performance due to the synergistic effect among transition metal ions. Compared to the corresponding hydroxide precursor (NiCoMn–OH) and other controlled sulfides with varying ratios of Ni/Co/Mn, the optimized NiCoMn–S nanosheets demonstrated higher C_s (2098.2 F/g). Furthermore, an asymmetric Sc (ASC) was assembled using the NiCoMn–S nanomaterials. This ASC exhibited a maximum E_s of 50.0 Wh/kg at 850.0 W/kg.

To create hybrid Scs that possess exceptional electrochemical properties, it is crucial to employ materials in negative and positive electrodes with superior characteristics. A recent study introduces a novel approach for constructing a hybrid Sc by utilizing metal sulfides and iron oxide as positive and negative electrodes.^[63] The synthesis of triple-shelled hollow spheres of nickel-cobalt-manganese sulfides (NCMS) is achieved via calcination and post-sulfurization. The sulfurization was achieved via dissolving the reaction mixture, sodium sulfide (0.39 g) in 15 mL of water, and then 25 mg of Ni–Co–Mn hydroxyl carbonate powder was dispersed into the solution. The resulting mixture was transferred into the autoclave and subjected to heating at 160 °C for a duration of 5 hours. After cooling down the precipitate was separated, washed, and subsequently dried overnight at 60 °C as presented in Figure 12(d). The transformation of the sheet-like morphology into a nanoparticle-like structure indicates the successful sulfidation process as depicted in Figure 12(e). This alteration in structural appearance strongly indicates the achievement of sulfidation. The positive electrode, NCMS-350, synthesized at 350 °C, exhibits an exceptional specific capacity of 797 C/g (depicted in Figure 12f), and impressive rate capability with 79.5% retention at 20 A/g. The negative electrode is composed of Fe₃O₄/N–rGO, synthesized via a hydrothermal process without subsequent calcination, demonstrating a maximum specific capacity of 454 C/g. Notably, when these electrodes are combined in the NCMS-350//Fe₃O₄/N–rGO hybrid configuration, the device achieves a remarkable E_s of 67.9 Wh/kg at 474 W/kg. These promising outcomes highlight a straightforward approach to optimizing and integrating electrode materials, leading to the development of high-performance hybrid Scs capable of efficient energy storage.

3.3. Sulfurization of other electrode material

N. Karthik et al. developed arrays of nickel cobalt layered double hydroxide nanosheets doped with sulfur (S-LDH/SS) on a stainless steel substrate for applications in electrocatalytic

hydrogen evolution reaction (HER) and Scs.^[64] SEM morphologies of stainless steel (SS) and LDH/SS show that the S-LDH deposition, a noticeable alteration in the SS surface is apparent, leading to the formation of a dense layer comprising interconnected nanosheet arrays with spacious pores in S-LDH/SS. The SEM images reveal a mixed arrangement of deposited nickel and cobalt double hydroxide, indicating differing reduction potentials for Ni²⁺ and Co²⁺ ions during CV. The porous texture facilitates enhanced electrolyte contact, establishing a broad contact area across the material. Figure 13(a) displays the cyclic voltammetry (CV) curves of S-LDH/SS obtained at different scan speeds within the voltage range of 0 to 0.50 V vs. Ag/AgCl. Irrespective of the scan speed, the CV curves consistently reveal two distinctive redox peaks around 0.36 and 0.18 V vs. Ag/AgCl, indicating a Faradaic behavior resembling that of a battery-like capacitor. In Figure 13(b), the GCD curves of S-LDH/SS at various are depicted. The non-linear shape of the GCD curves, coupled with the presence of redox peaks at 0.32 V (oxidation) and 0.21 V (reduction) vs. Ag/AgCl (at 1 A/g), suggests a charging and discharging mechanism reminiscent of a battery-like behaviour for S-LDH/SS. The specific capacities of S-LDH/SS calculated at different J_s are as follows: 232, 163, 121, 92, and 75 C/g (mAh/g). In Figure 13(c), all Nyquist plots of S-LDH/SS exhibit a single semicircle that originates from high frequencies and gradually moves towards low frequencies, indicating the R_{ct} . As the overpotential increases from +0.10 to –0.70 V vs. RHE, the semicircle diameter significantly decreases, indicating a reduction in the HER R_{ct} . At a scan rate of 5 mV/s and an overpotential of –0.70 V, the enhanced S-LDH/SS electrode demonstrates a battery-like behaviour, achieving a maximum 344 C/g (95.5 mAh/g) value of specific capacity with outstanding cycle stability and capacity retention. The S-LDH/SS electrode conductivity is assessed using electrochemical impedance spectroscopy (EIS) across various HER overpotentials (0.10, 0.30, 0.50, and 0.70 V vs. RHE), revealing enhanced performance. Overall, the developed electrode exhibits significant potential for future applications in energy conversion and storage.

Sc potential electrode material, the metal phosphides have a high storage capacity and conductivity. Their short-term cycle stability, though, is causing them problems. The total electrochemical performance of metal phosphides is successfully improved here by establishing a good sulfurization technique.^[65] The electrochemical performance of cobalt phosphate/carbon cloth electrodes CoP/CC and cobalt/(phosphate, sulfide)/carbon cloth electrodes Co(P, S)/CC electrodes in an alkaline electrolyte was investigated by AM Elshahawy et al. STEM HAADF (high-angle annular dark field) proves effective in structure imaging, offering a contrast that can be interpreted in terms of mass thickness or Z contrast. The porous structure is distinctly observable due to the contract variation. It's worth noting that while this description acknowledges the visibility of the porous structure, it lacks specific details regarding the morphology of the nanowires. The CV curves for both electrodes at a 5 mV/s scan rate are shown in Figure 13(d). The sulfur in the CoP/CC structure is responsible for additional redox peaks that may be seen at the potentials of +0.28,

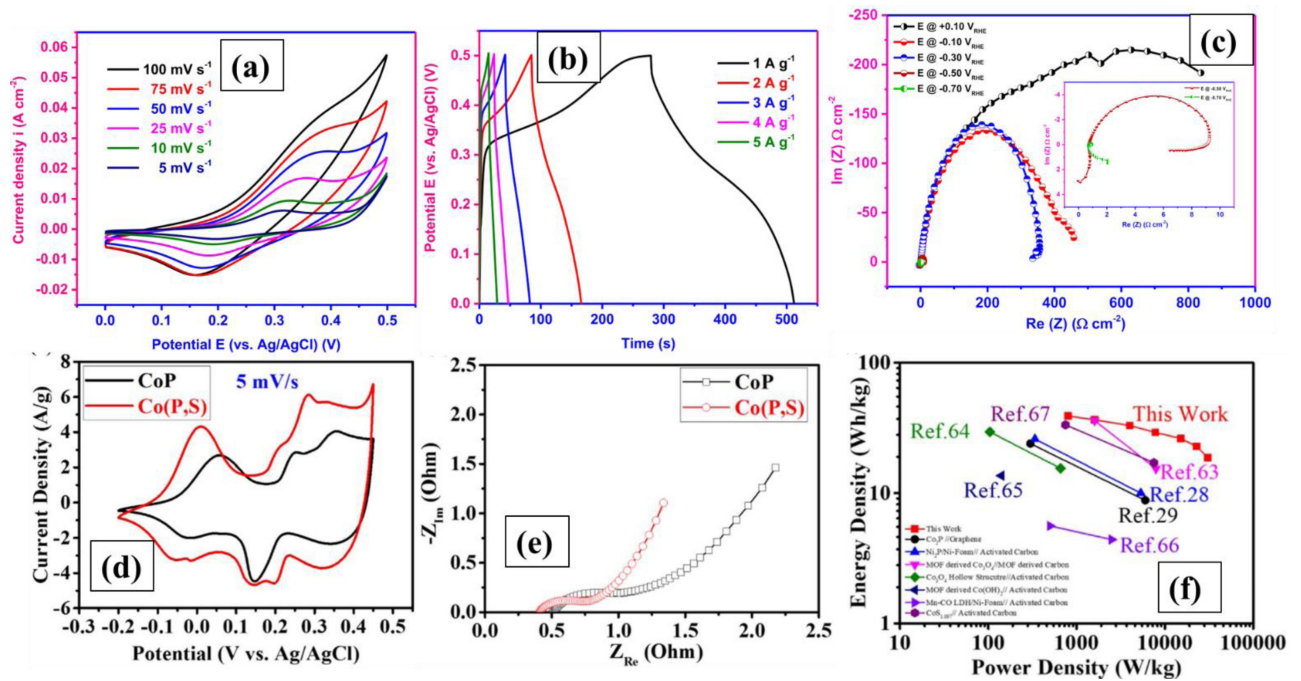


Figure 13. a) S-LDH/SS CV profiles, b) GCD curves and c) Nyquist EIS plot, reproduced from ref. [64] Copyright (2019) Elsevier. d) CV curves (5.0 mV/s), e) the EIS plot and f) the Ragone plot, illustrates the E_s and P_s performance of the hybrid device, reproduced from ref. [65] Copyright (2017) Elsevier.

+0.19, and -0.0175 V. As depicted in Figure 13(e), the introduction of sulfur doping enhances the conductivity of CoP, leading to a reduction in the passivation layer on its surface. This improvement facilitates better charge transfer and ion diffusion within the material. Figure 13(f) shows the Ragone plot of E_s against P_s for hybrid Sc cells, depicting high E_s of 39 Wh/kg at a P_s of 0.8 kW/kg in 175.4 s. The stronger conductivity of Co(P, S)/CC is demonstrated by the electrode's R_{eq} , which is 0.51 ohm less than that of CoP/CC. The CoP/CC has a capacity that is 1.78 times less efficient than the derived nanotubes, which have a capacity of 1.0 A/g (165.82 mAh/g (342.8 F/g)). At 20 A/g, Co(P, S) and CoP had rate capabilities of 66 and 71.42%, respectively. The great profited outcomes show that the unique method of sulfur addition to metal phosphide opens up new directions for creating highly proficient electrodes.

Researchers discovered that the energy storage capability of Nickel cobalt fluoride decorating ammonia ions (NCNF) can be enhanced through copper decoration and sulfidation.^[66] In the absence of copper decoration, subjecting the aggregated particles to sulfidation at 160°C led to their transformation into individual nanoparticles, accompanied by a partial conversion of NCNF to cobalt sulfide. The optimized sulfide derived from NCNF demonstrated the highest Cs of 1666.1 F/g (277.7 mAh/g), whereas the untreated NCNF electrode only exhibited 519.8 F/g (277.7 mAh/g) Cs. This notable improvement can be attributed to the partial sulfidation process, which leverages the excellent electrocapacitive properties of NCNF and the superior conductive nature of sulfide. By employing a symmetric energy storage architecture with optimized

sulfide electrodes derived from NCNF, a maximum E_s of 8.64 Wh/kg was attained at 2.16 kW/kg.

Despite numerous modifications, including heteroatom doping, to enhance the performance of transition metal oxides/hydroxides in electrocatalytic water splitting and Scs, their full potential has not yet been realized. In a recent study, cobalt hydroxide was subjected to a series of treatments involving calcination, sulfidation, and phosphorization.^[67] The cobalt hydroxide was initially prepared through an uncomplicated electrodeposition process on nickel foam at -1.0 V. The morphology of Co(OH)_2 , Co_3O_4 , Co_3S_4 and CoP analysis of the synthesized samples was conducted through SEM. The SEM images of the catalyst samples reveal an intricately interconnected porous network structure. At lower magnifications, a distinctive wrinkles-like configuration is observed, featuring open nanopores that have the potential to enhance electron/ion interaction during electrocatalytic or supercapacitor activities. Subjection to CV characterization reveals redox active nature as well as the sound rate capability of sulfidized material (Figure 14a). Experimental findings revealed that the resulting cobalt sulfide exhibited the highest Cs of 3.7 F/cm 2 , accompanied by the largest E_s of 0.144 Wh/cm 2 and a high P_s of 8.28 W/cm 2 proclaiming the dominance of sulfidation (Figure 14b, c). The enhanced electrochemical performance can be attributed to the incorporation of sulfur atoms. These S-atoms alter the electronic properties of the Co-sites, leading to increased conductivity compared to the conductive nature induced by P-atoms in CoP. Overall, the as-synthesized Co-based materials, particularly CoS, demonstrated remarkable electrocatalytic activity and electrochemical stability. This makes them cost-

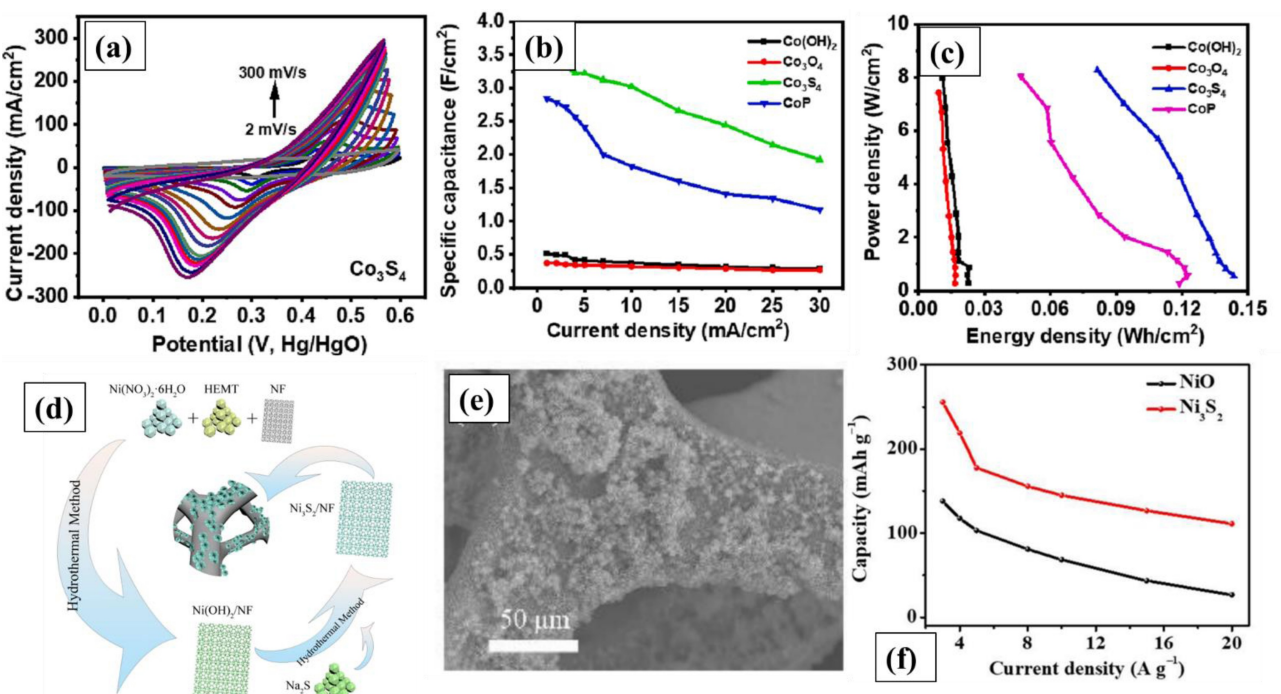


Figure 14. a) CV curves, b) Cs trend and c) achieved Es and Ps. Reproduced from ref. [67], Copyright (2023) Elsevier. d) Schematic of synthesis approach, e) SEM and f) achieved capacity trend, reproduced from ref. [68] Copyright (2023) The Author(s).

effective and environmentally friendly alternatives for energy storage and water-splitting applications.

Ni_3S_2 NWs possess high Cs and are considered a promising choice for SC electrodes. However, their limited applications stem from their low chemical stability and poor electrical conductivity. To overcome these limitations, a recent presents a novel one-step sulfidation method for the direct fabrication of Ni_3S_2 nanowires on a Ni foam substrate using a hydrothermal method.^[68] SEM image depicts the morphologies of NiO/NF and $\text{Ni}_3\text{S}_2/\text{NF}$ electrodes. Post-sulfidation, Ni_3S_2 nanowires uniformly disperse on NF, forming a secure anchor to NF network. $\text{Ni}_3\text{S}_2/\text{NF}$ exhibits a stronger interconnection between NWs and NF compared to NiO/NF, enhancing its resilience to rigorous redox reactions in alkaline electrolytes and contributing to improved cycling stability. Figure 14(d) illustrates the fabrication strategy for constructing a binder-free self-supported nanoarray of hierarchical Ni_3S_2 nanowires (NWs) on a three-dimensional (3D) NF surface. The process begins with the synthesis of $\text{Ni}(\text{OH})_2/\text{NF}$ through a hydrothermal method. Subsequently, Na_2S is utilized as the source of sulfur, leading to the hydrolysis of Na_2S and the release of S^{2-} ions. Under hydrothermal conditions, the Ni^{2+} and S^{2-} ions readily combine to precipitate Ni_3S_2 .^[29] Eventually, the reaction between $\text{Ni}(\text{OH})_2$ and Na_2S yields the formation of Ni_3S_2 nanowires (NWs) (Figure 14e). The method offers a simple and cost-effective approach for synthesizing electrode materials for SCs (SCs), with the goal of optimizing energy storage. The feasibility of utilizing binder-free electrodes to achieve high-performance SC was investigated. The electrode demonstrated a high specific capacity of 255.3 mAh/g, (Figure 14f) excellent cyclic preservence (72.17%

after 5000 cycles) and superior rate capability (2.9 times higher than the NiO/NF electrode). The developed hydrothermal reaction-based self-growth method for Ni_3S_2 electrodes on three-dimensional substrates could potentially be extended to fabricate electrodes using various other transition metal compounds.

Recently a novel approach to manufacturing NiS_x supercapacitor electrodes, produced from Ni-foam using a one-zone sulfidization technique was reported.^[69]

The successful creation of NiS_x ($x=1$ and 2) was confirmed through the utilization of scanning electron microscopy (SEM) and X-ray diffractometry (XRD). Electrodes prepared at 400 °C and 250 °C exhibited specific capacitances of 105 mF/cm² and 510 mF/cm², respectively. The presence of anodic and cathodic peaks suggests that both samples, prepared at varying sulfidation temperatures, possess a pseudo-capacitive charge storage mechanism. It is hypothesized that the significantly higher capacitance observed in the sample prepared at 250 °C can be attributed to a greater density of nickel sulfide nanoflakes within its structure.

H. Zeng has developed an effective method to synthesize Ni–Co–Mo polycrystalline sulfide (NiCoMoS) by employing doping engineering combined with chemical transformation.^[70] The synthesis involves designing and fabricating polycrystalline NiCoMoS on a Ni foam substrate, utilizing a simple post-sulfidation process. To elaborate, well-designed polycrystalline NiCoMoO₄ precursor by introducing Co ions into the NiMoO₄ structure were prepared with ordered nanoneedle arrays, forming a three-dimensional architecture. NiCoMoS (2.0) array, integrated onto the NF as a self-supporting electrode, exhibits

exceptional electrochemical performance. It demonstrates a high specific charge capacity of 920.0 C/g, excellent long-term stability and rate capability. Additionally, when combined with activated carbon in a hybrid device, the assembled NiCoMoS//activated carbon configuration delivers satisfactory supercapacitor performance. It achieves an Es of 35.2 Wh/kg at a Ps of 800.0 W/kg. This innovative strategy opens up new possibilities for discovering additional polymetallic sulfides with enhanced active sites, thereby broadening their potential applications in energy-related fields.

4. Analysed Fascinating Attributed

The sulfurization of electrode materials offers several advantages in energy storage applications. First and foremost, sulfur is an abundant and inexpensive element, making it a cost-effective choice. Additionally, it exhibits high theoretical specific capacity, meaning it can store a large amount of energy per unit mass. This makes sulfur-based electrodes attractive for high-energy storage applications. The promising advent presented via sulfurization of electrode material are the following.

4.1. Carbonaceous materials

Carbonaceous materials possessing surface functional groups, exceptional chemical stability and excellent electrical conductivity, such as carbon nanotube, graphene, and activated carbon, represented highly promising options for implementing Sc.^[71] These attributes facilitate efficient charge accumulation at the electrode interface, thereby enhancing its capacitive performance. Sulfur possesses lone pair of electrons and when introduced in electrode material influences the pore size, structure and capacitance behaviour of electrode materials. Conjugating the lone pair on the heteroatoms with the carbon framework system can enhance the wettability of electrolytes and improve surface activity, including the faradaic nature.^[72] Enhancements in the redox properties directly contribute to the elevation of capacitance, conductivity, and rate capability of electrode materials. Sulfur species have been discovered to boost the effectiveness of charge storage in tiny pores via EDLC in sulphuric acid.^[73] This is because they rearrange the charge density in carbonaceous surroundings to a more positive state. In addition, the surface morphology of sulphurized material production of flakes with hierarchically porous (depicted in the SEM) which concluded that more diffusion of ions can take place in it, enhances the electrical conductivity of electrode material.^[74] Sulfurization was found to modify the surface chemistry and structure of activated carbon, resulting in improved electrochemical performance. In energy storage applications, it expands the surface area and adds more active sites, resulting in increased charge storage capacity and quicker charge/discharge rates.^[75] High surface area and porosity are characteristics of activated carbon, allowing for efficient sulfur loading during the sulfurization process. This makes it possible to include a significant amount of sulfur into the carbon

network, leading to higher energy storage capacities in batteries or Scs. Sulfurization enhances the stability and cycle life of activated carbon electrodes. The sulfur species introduced during the process can chemically interact with the carbon framework, inhibiting the dissolution and diffusion of active materials during cycling, thereby mitigating capacity decay and extending the lifespan of the electrode.^[76] Porous carbon possesses a tenable pore structure that can be further customized through sulfurization. Sulfur species can change the pore size distribution and introduce more mesopores or micropores, which can improve ion transport and electrolyte accessibility, eventually enhancing the electrochemical performance.^[77] In addition, the versatility of sulfurization methods allows for the selection of an appropriate sulfurization technique based on the specific requirements of the desired application. Moreover, the Sulfurization of activated carbon is compatible with existing carbon-based technologies and manufacturing processes. It can be seamlessly integrated into the production of carbon-based electrodes, allowing for efficient scaling and commercialization of sulfurized activated carbon materials.^[44] The use of carbonaceous materials as a precursor and the sulfurization process itself is environmentally friendly compared to some conventional electrode materials. Activated carbon is derived from renewable resources and sulfurization can be carried out using green and non-toxic sulfur sources, promoting sustainability in energy storage applications.

4.2. Non-carbonaceous material

Sulfurization modifies the surface of electrode materials, and enhances the active sites available for charge transfer, resulting in higher capacity, better efficiency, and improved electrochemical performance for energy storage devices.^[76] The sulfur-based compounds or sulfur-containing polymers, as electrode materials hold high theoretical energy densities. The affordability contributes to the scalability and commercial viability of energy storage technologies. Sulfurization reduces the reliance on expensive and environmentally harmful transition metal-based electrode materials, such as cobalt or nickel. The incorporation facilitates the advancement of environmentally sustainable and eco-friendly solutions for storing energy.^[78] Numerous electrode materials, including metals, and metal oxides, can be sulfurized. With this flexibility, electrodes may be customized to have the conductivity, surface area, and stability needed for a given application. Sulfur-based electrode materials can be integrated into existing battery manufacturing processes with minimal modifications.^[79] This compatibility facilitates the adoption of sulfurization techniques without significant disruptions to current production methods. Sulfurization can impart multifunctional properties to electrode materials. For instance, sulfur-based electrodes may have high catalytic activity, allowing for the simultaneous storage of energy and catalysis for uses like fuel cells or water splitting. The features such as enhanced electrochemical performance, high sulfur loading, improved stability and cycle life, tailored pore

structure, versatile sulfurization methods, compatibility with existing carbon-based technologies, cost-effectiveness, environmental sustainability, design flexibility, compatibility with existing infrastructure, and potential for multi-functionality braces their future of sulfurization in the advancement of technology.^[80,81] These features make sulfurization a promising strategy for advancing Sc technologies, the promising future of energy storage.

Different discussed sulfurized electrode materials and their profited electrochemical attributes are presented in Table 1.

5. Future Challenges

The sulfurization of electrode materials for supercapacitor applications presents several research challenges that need to be addressed for further advancements in the field. Sulfurization processes can be complex, involving multiple reaction parameters such as temperature, time, and sulfur precursor concentration. Controlling these variables is crucial to ensure consistent and reproducible results. Variations in reaction conditions may lead to inconsistent material properties, affecting the overall performance of supercapacitors. Sulfurization may not be universally applicable to all electrode materials. Some materials may react unfavorably with sulfur precursors, leading to phase segregation, structural degradation, or loss of electrical conductivity. Identifying compatible electrode materi-

Table 1. Electrochemical outcomes of multiple sulfurized electrode materials.

Sample	Synthesis approach	Capacitance/ capacity	Energy density [Wh/kg]	Power density [W/kg]	Stability (Cycles)	Reference
AC SAC	Thermal evaporation	82.3 F/g (0.07 A/g)	–	–	90 % (2000)	[43]
CoS2@NiMo2S4/NF	Co-precipitation method	802 C/g (1 A/g)	32.1	1130.3	87.2 % (10,000)	[81]
Ni3S2 nanowires	Hydrothermal	255.3 mAh/g	–	–	72.17 % (5000)	[68]
NSAC and PANI	Hydrothermal	578 F/g (A/g)	80	500	72 % (2000)	[32]
P-S-CNTs	Chemical vapor deposition	120.2 F/g (100 mA/cm ²)	–	–	95.5 % (2000)	[46]
cobalt hydroxide	Carbonization	3.7 F/cm ²	0.144 Wh/cm ²	8.28 W/cm ²	95 % (500)	[65]
S-PC-50	Carbonization	320 F/g (0.2 A/g)	8.2	50	99 % (10,000)	[48]
NSG-10	Activation method	33.7 F/g (0.2 A/g)	4.51	2785	82.0 % (10,000)	[49]
CoNiWO ₄ /P-S-GNS	Hydrothermal	723.8 F/g (0.5 A/g)	100.8	3234.2	95.5 % (7500)	[50]
N/S-3DGH	Hydrothermal process	1063 C/g (1 A/g)	6.25	500	76 % (6000)	[51]
NiS _x (x = 1 and 2)	Solvothermal method	510 mF/cm ²	–	–	83.54 % (5000)	[69]
NS-Gm05	Hydrothermal	431 F/g (0.5 A/g)	–	–	92 % (1000)	[52]
RGO-S	Improved hummers method	113.8 mAh/g (0.5 A/g)	35.2	375	99 % (10,000)	[53]
SG-MnO _x	Environmentally friendly synthesis	67.95 F/g (2 A/g)	21.23	1.5 k	81.2 % (5000)	[54]
NSG-210	Hydrothermal	227.94 F/g (10 mV/s)	8.3	510	83 % (25,000)	[55]
N/S-rGA-1	Hydrothermal	180.5 F/g (1 A/g)	75	0.9 k	80 % (5000)	[56]
S-RGO-1000	Hydrothermal	270 F/g (5 mV/s)	–	–	100.8 % (10,000)	[57]
RGO-S/MnO ₂ //AC-PS	Hydrothermal	178.74 F/g (1 A/g)	71.74	850	94.5 % (10,000)	[58]
NiCoMoS	Green method/hydrothermal post-sulfurization	920 C/g	35.2	800	91.3 % (5000)	[70]
NCMS	post-sulfurization	1885 F/g (0.3 A/g)	67.9	474	75.56 % (4000)	[63]
S-LDH/SS	Co-electrodeposition technique	344 C/g (5 mV/s)	–	–	Good stability	[64]
NiCo ₂ S ₄ @C	Thermal sulfidation	948.9 C/g (1.0 A/g)	43.8	799.1	81.9 % (50,000)	[61]

als and optimizing the sulfurization process for each material is essential that craves further efforts for successful implementation. The incorporation of sulfur into electrode materials needs to be carefully optimized. Insufficient sulfur content may limit the pseudocapacitive effect, while excessive sulfur loading can cause detrimental effects on the electrode's electrical conductivity and stability. While sulfurization techniques have demonstrated promising results at the laboratory scale, scaling up the process to industrial levels presents challenges. Achieving uniform and controlled sulfurization across large-area electrodes and maintaining consistent quality during mass production can be technically demanding. Sulfurization can improve the stability of electrode materials, but long-term stability and cycling performance need further investigation. Understanding the degradation mechanisms and designing electrode materials with improved stability and durability under prolonged cycling conditions are vital for practical applications. The choice of electrolyte used in supercapacitors can significantly influence the performance and stability of sulfurized electrodes. Compatibility issues between the sulfurized materials and certain electrolytes may arise, necessitating the development of suitable electrolyte systems and further consideration. Although sulfur is an abundant element, ensuring a sustainable and cost-effective supply chain for sulfur-based precursors is essential. Developing efficient sulfurization processes that minimize raw material consumption and optimize energy usage will contribute to the economic viability of sulfurized electrode materials. Assessing the environmental impact of the sulfurization process and sulfurized electrode materials is important for sustainable energy storage technologies. Investigating the potential for recycling or safe disposal of sulfur-containing materials is essential to minimize the environmental footprint. A comprehensive understanding of the sulfurization mechanism is necessary to optimize the process and tailor the properties of sulfurized electrode materials. Investigating the kinetics, phase transformations, and sulfur incorporation mechanisms will provide insights into the fundamental aspects of the sulfurization process. Identifying suitable sulfur precursors and optimizing their concentration, reactivity, and compatibility with different electrode materials is crucial. Exploring a wide range of sulfur sources and their influence on the properties of the sulfurized materials can lead to the development of novel and efficient sulfurization strategies. Overcoming these obstacles will pave the way for the utilization of sulfurization as a viable and sustainable approach in the field of energy storage.

6. Conclusions

In conclusion, the sulfurization process has been proven to be an effective method for enhancing the electrochemical attributes of electrode materials, leading to improved supercapacitor performance. Through a comprehensive literature review, it was evident that sulfurization can significantly increase the specific capacitance, strength cycling stability, and rate capability along with tuned conductivity of electrode materials. The incorporation of sulfur into the electrode matrix was found to promote

the pseudocapacitive behavior, facilitating the reversible Faradaic redox reactions and increasing the overall energy storage capacity. The versatile approaches of process allow precise control over the sulfur content, morphology, and distribution within the electrode structure, enabling tailored electrode designs for specific applications. Additionally, the findings presented here contribute to the advancement of energy storage technologies and offer new avenues for the development of high-performance supercapacitors with increased storage capability and improved efficiency. Further research and optimization in this field are crucial to fully exploit the benefits of sulfurization and pave the way for its practical implementation in energy storage devices.

Acknowledgements

The authors extend their appreciation to the Deanship of Scientific Research at King Khalid University for funding this work through large group Research Project under grant number RGP.2/575/44.

Conflict of Interests

The authors declare no conflict of interest.

Data Availability Statement

The data that support the findings of this study are available on request from the corresponding author. The data are not publicly available due to privacy or ethical restrictions.

Keywords: supercapacitor • sulfurization • improved conductivity • specific energy • specific power

- [1] S. A. Hussain, F. Razi, K. Hewage, R. J. E. Sadiq, *Energy*. **2023**, *275*, 127487.
- [2] E. Erdem, *Environmental Progress & Sustainable Energy*. **2021**, *40*, e13545.
- [3] V. Litvinenko, I. Bowbrick, I. Naumov, Z. J. J. o. C. P. Zaitseva, *Journal of Cleaner Production*. **2022**, *338*, 130530.
- [4] E. T. Sayed, A. G. Olabi, A. H. Alami, A. Radwan, A. Mdallal, A. Rezk, et al., *Energies*. **2023**, *16*, 1415.
- [5] A. U. Ammar, I. D. Yildirim, F. Bakan, E. Erdem, *Beilstein J. Nanotechnol.* **2021**, *12*, 49–57.
- [6] M. Tuncer, F. Bakan, H. Gocmez, E. Erdem, *Nanoscale*. **2019**, *11*, 18375–81.
- [7] M. Buldu-Akturk, M. Toufani, A. Tufani, E. Erdem, *Nanoscale*. **2022**, *14*, 3269–78.
- [8] J. Huang, Y. Xie, Y. You, J. Yuan, Q. Xu, H. Xie, et al., *Adv. Funct. Mater.* **2023**, *33*, 2213095.
- [9] A. Philip, A. R. Kumar, *Renewable Sustainable Energy Rev.* **2023**, *182*, 113423.
- [10] Z. Pan, S. Yu, L. Wang, C. Li, F. Meng, N. Wang, et al., *Nanomaterials*. **2023**, *13*, 1744.
- [11] D. Wei, Y. Cao, L. Yan, H. Gang, B. Wu, B. Ouyang, et al., *ACS Appl. Mater. Interfaces* **2023**, *15*, 24427–24436.
- [12] F. Su, F. Xing, X. Wang, F. Liu, L. Zhang, Z.-S. Wu, *Energy Environ. Sci.* **2023**, *16*, 222–30.
- [13] W. Xi, Y. Zhang, J. Zhang, R. Wang, Y. Gong, B. He, et al., *J. Mater. Chem. C* **2023**, *11*, 2414–29.

- [14] M. Z. Iqbal, J. Khan, A. M. Afzal, S. Aftab, *Electrochim. Acta* **2021**, *384*, 138358.
- [15] M. Z. Iqbal, J. Khan, *Electrochim. Acta* **2021**, *368*, 137529.
- [16] A. Amiri, A. Bruno, A. A. Polycarpou, *Carbon Energy* **2023**, *5*, e320.
- [17] I. Melkiyur, Y. Rathinam, P. S. Kumar, A. Sankaiya, S. Pitchaiya, R. Ganeshan, et al., *Renewable Sustainable Energy Rev.* **2023**, *173*, 113106.
- [18] K. A. Sammed, A. Farid, S. Mustafa, A. Kumar, M. Tabish, A. A. Khan, et al., *Fuel Process. Technol.* **2023**, *250*, 107896.
- [19] S. R. Ka, C. S. Rout, *J. Mater. Chem. A* **2023**, *11*, 5495–5519.
- [20] A. Hayat, M. Sohail, A. El Jery, K. M. Al-Zaydi, S. Raza, H. Ali, et al., *Mater. Today* **2023**, *64*, 180–208.
- [21] J. C. Janardhanan, N. T. Padmanabhan, S. C. Pillai, H. John, *ACS Sustainable Chem. Eng.* **2023**, *11*, 6890–902.
- [22] M. Devi, B. Moorthy, R. Thangavel, *Sustain. Energy Fuels* **2023**, *7*, 3776–3795.
- [23] K. Dericiler, M. Hezarkhani, I. E. Tabrizi, S. Dogan, I. Berktaş, E. Erdem, et al., *Appl. Compos. Mater.* **2023**, *1*–17.
- [24] P. Ondrejka, M. Sojkova, V. Kotok, P. Novak, I. Hotovy, M. Kemény, et al., *Mater. Res. Express* **2023**, *10*, 065508.
- [25] N. Sapkota, S. Chiluwal, P. Parajuli, A. Rowland, R. Podila, *Adv. Sci.* **2023**, *2206901*.
- [26] S. Ghosh, S. S. Withanage, B. Chamlagain, S. I. Khondaker, S. Harish, B. B. Saha, *Energy* **2020**, *203*, 117918.
- [27] X. Ao, Y. Gu, C. Li, Y. Wu, C. Wu, S. Xun, et al., *Appl. Catal. B* **2022**, *315*, 121586.
- [28] X. Huang, J. Liu, Z. Huang, X. Ke, L. Liu, N. Wang, et al., *Electrochim. Acta* **2020**, *333*, 135493.
- [29] K. Thompson, J. Choi, D. Neupane, S. R. Mishra, F. Perez, R. K. Gupta, *Surf. Coat. Technol.* **2021**, *421*, 127435.
- [30] L. Yang, T. Wang, D. Wu, *Chin. J. Chem.* **2020**, *38*, 1123–31.
- [31] N. Poompiew, P. Pattananuwat, Potiyaraj, *RSC Advances* **2021**, *11*, 25057–67.
- [32] S. Uppugalla, Srinivasan, *Journal of Solid State Electrochemistry* **2019**, *23*, 295–306.
- [33] J. Huo, P. Zheng, X. Wang, S. J. A. S. S. Guo, *Appl. Surf. Sci.* **2018**, *442*, 575–80.
- [34] Y. Hu, J. Zhang, D. Wang, J. Sun, L. Zhang, Y. Liu, et al., *Particuology* **2019**, *45*, 66–73.
- [35] H. Chen, J. Wang, F. Liao, X. Han, Y. Zhang, C. Xu, et al., *Ceram. Int.* **2019**, *45*, 11876–82.
- [36] H. Deng, M. Zhu, T. Jin, C. Cheng, J. Zheng, Qian, *International Journal of Electrochemical Science* **2020**, *15*, 16–25.
- [37] N. Karthik, T. N. J. I. Edison, R. Atchudan, M. G. J. J. o. A. Sethuraman, *Compounds* **2017**, *729*, 126–36.
- [38] J. Acharya, B. G. S. Raj, T. H. Ko, M.-S. Khil, H.-Y. Kim, B.-S. J. i. j. o. h. e. Kim, *International Journal of Hydrogen Energy* **2020**, *45*, 3073–85.
- [39] C. Bathula, I. Rabani, A. Kadam, H. Opoku, S. A. Patil, N. K. Shreshta, et al., *J. Colloid Interface Sci.* **2022**, *606*, 1792–9.
- [40] C. Han, J. Andersen, S. C. Pillai, R. Fagan, P. Falaras, J. A. Byrne, et al., Chapter green nanotechnology: development of nanomaterials for environmental and energy applications. *Sustainable nanotechnology and the environment: Advances and achievements: ACS Publications 2013*, p. 201–29.
- [41] J. Huo, Y. Ren, Y. Xue, Y. Liu, S. J. J. o. A. Guo, *Compounds* **2021**, *868*, 159183.
- [42] H. Tang, D. Yan, T. Lu, L. J. E. A. Pan, *Electrochim. Acta* **2017**, *241*, 63–72.
- [43] Y. Huang, S. L. Candelaria, Y. Li, Z. Li, J. Tian, L. Zhang, et al., *J. Power Sources* **2014**, *252*, 90–7.
- [44] A. Elmouwahidi, J. Castelo-Quibén, J. F. Vivo-Vilches, A. F. Pérez-Cadenas, F. J. Maldonado-Hódar, F. J. C. E. J. Carrasco-Marín, *Chem. Eng. J.* **2018**, *334*, 1835–41.
- [45] Y. Bojjoo, Y. Cheng, H. Zhong, H. Tian, J. Pan, V. K. Pareek, et al., *Carbon* **2017**, *116*, 490–9.
- [46] J. H. Kim, Y.-i. Ko, Y. A. Kim, K. S. Kim, C.-M. J. J. o. A. Yang, *Compounds* **2021**, *855*, 157282.
- [47] X. Ma, G. Ning, Y. Kan, Y. Ma, C. Qi, B. Chen, et al., *Electrochim. Acta* **2014**, *150*, 108–13.
- [48] J. Tian, H. Zhang, Z. Liu, G. Qin, Z. J. I. J. o. H. E. Li, *Journal of Hydrogen Energy* **2018**, *43*, 1596–605.
- [49] M. Karuppannan, Y. Kim, Y.-E. Sung, O. J. J. J. o. A. E. Kwon, *J. Appl. Electrochem.* **2019**, *49*, 57–66.
- [50] A. S. Rajpurohit, N. S. Punde, C. R. Rawool, A. K. J. C. E. J. Srivastava, *Chem. Eng. J.* **2019**, *371*, 679–92.
- [51] W. Zhang, Z. Chen, X. Guo, K. Jin, Y. Wang, L. Li, et al., *Electrochim. Acta* **2018**, *278*, 51–60.
- [52] D. Wu, T. Wang, L. Wang, D. J. M. Jia, *M. Materials* **2019**, *290*, 109556.
- [53] D. J. Tarimo, K. O. Oyedotun, A. A. Mirghni, N. J. I. J. o. H. E. Manyala, *Int. J. Hydrogen Energy* **2020**, *45*, 13189–201.
- [54] Q. Lv, H. Hao, M. Ge, W. J. J. o. A. Li, *Compounds* **2020**, *819*, 152970.
- [55] L. Cheng, Y. Hu, D. Qiao, Y. Zhu, H. Wang, Z. J. E. A. Jiao, *Electrochim. Acta* **2018**, *259*, 587–97.
- [56] Y. Chen, L. Sun, Z. Liu, Y. Jiang, K. J. M. C. Zhuo, *Physics* **2019**, *238*, 121932.
- [57] X. Zhang, R. J. A. S. S. Zhang, *Appl. Surf. Sci.* **2019**, *479*, 1039–47.
- [58] D. J. Tarimo, K. O. Oyedotun, A. A. Mirghni, N. F. Sylla, N. J. E. A. Manyala, *Electrochim. Acta* **2020**, *353*, 136498.
- [59] A. Alabadi, S. Razzaque, Z. Dong, W. Wang, B. J. J. o. P. S. Tan, *J. Power Sources* **2016**, *306*, 241–7.
- [60] Y. Wang, M. Zhang, D. Pan, Y. Li, T. Ma, J. J. E. A. Xie, *Electrochim. Acta* **2018**, *266*, 242–53.
- [61] W. Cao, Y. Liu, F. Xu, Q. Xia, G. Du, Z. Fan, et al., *Electrochim. Acta* **2021**, *385*, 138433.
- [62] C. Kang, L. Ma, Y. Chen, L. Fu, Q. Hu, C. Zhou, et al., *Chem. Eng. J.* **2022**, *427*, 131003.
- [63] T. L. Tamang, S. Sahoo, J.-J. Shim, *J. Power Sources* **2023**, *572*, 233107.
- [64] N. Karthik, T. N. J. I. Edison, R. Atchudan, D. Xiong, Y. R. J. J. o. E. C. Lee, *J. Electroanal. Chem.* **2019**, *833*, 105–12.
- [65] A. M. Elshahawy, C. Guan, X. Li, H. Zhang, Y. Hu, H. Wu, et al., *Nano Energy* **2017**, *39*, 162–71.
- [66] P.-Y. Lee, L.-Y. Lin, S. Yougbare, *J. Solid State Chem.* **2022**, *313*, 123345.
- [67] E. A. Mehari, M. A. Asare, W. Lin, K. Mensah-Darkwa, A. Kumar, D. Neupane, et al., *Results in Chemistry* **2023**, *5*, 100879.
- [68] Q. Xia, L. Si, K. Liu, A. Zhou, C. Su, N. M. Shinde, et al., *Molecules* **2023**, *28*, 4307.
- [69] P. Ondrejka, M. Sojková, V. Kotok, O. Zima, M. Kemény, P. Novák, et al., Sulfurization of Ni-foam as a binder-free supercapacitor electrode, *2022, 14th International Conference on Advanced Semiconductor Devices and Microsystems (ASDAM): IEEE*; 2022, p. 1–4.
- [70] K. Zhang, H.-Y. Zeng, K.-W. Ge, M.-X. Wang, H.-B. Li, *Inorg. Chem.* **2023**.
- [71] S. S. Ashok Kumar, S. Bashir, M. Pershaanaa, F. Kamarulazam, N. M. Saidi, Z. L. Goh, et al., *J. Mater. Sci.* **2023**, *58*, 6516–55.
- [72] D. Wu, T. Wang, L. Wang, D. Jia, *Microporous Mesoporous Mater.* **2019**, *290*, 109556.
- [73] S. Uppugalla, R. Pothu, R. Boddula, M. A. Desai, N. Al-Qahtani, *Emergent Materials*. **2023**, 1–10.
- [74] S. K. Sukhmani, S. D. Raut, T. Siddiqui, S. F. Shaikh, N. M. Shinde, R. S. Mane, *Mater. Res. Bull.* **2022**, *156*, 111975.
- [75] L. Wang, N. Zhou, *J. Energy Storage* **2022**, *53*, 105097.
- [76] F. B. Ahmed, D. Khalafallah, M. Zhi, Z. Hong, *Advanced Composites and Hybrid Materials* **2022**, *5*, 2500–14. Volume 5,

Pages

2500–2514.

- [77] S. Huang, Y. Ding, Y. Li, X. Han, B. Xing, S. Wang, *Energy Fuels* **2021**, *35*, 1557–66.
- [78] S. Zhao, Z. Yang, W. Xu, Q. Zhang, X. Zhao, X. Wen, *Electrochim. Acta* **2019**, *297*, 334–43.
- [79] S.-X. Yan, S.-H. Luo, H. Liu, L. Yang, Q. Wang, Y.-H. Zhang, et al., *Surf. Coat. Technol.* **2022**, *429*, 127980.
- [80] H. A. El-Sabban, S. Y. Attia, M. Diab, S. G. Mohamed, *J. Energy Storage* **2023**, *60*, 106593.
- [81] K. Zhang, X. Gao, F. Yao, Y. Xie, H. Bai, Y. Sun, et al., *J. Colloid Interface Sci.* **2023**, *650*, 105–111.

Manuscript received: August 23, 2023

Revised manuscript received: November 17, 2023

Accepted manuscript online: November 22, 2023

Version of record online: December 22, 2023